JANUS: A Constraint-Aware Hybrid Photonic Architecture with One-Hot Optical RNS Multiplication, High-Power Passive Fan-Out, and Bounded Exact-Precision Computation

Deepanshu Bhardwaj

Patent Application No.: 202611052791 (Patent Pending)

***Abstract*—Large-scale photonic accelerators are fundamentally constrained by analog precision collapse, optical loss accumulation, thermal drift, nonlinear wavelength interference, and the unsustainable static power requirements of thermo-optic routing meshes. Conventional photonic matrix multiplication architectures rely upon analog amplitude accumulation followed by high-speed analog-to-digital conversion, implicitly assuming that signal fidelity can scale with matrix dimension. However, for a 128×128 photonic multiply-accumulate operation using 8-bit operands, the accumulated output spans more than 8.3×10^6 discrete levels, requiring approximately 138 dB signal-to-noise ratio (SNR) for lossless analog recovery—a precision-throughput tradeoff that becomes increasingly impractical under realistic shot noise, thermal noise, and ADC bandwidth constraints at multi-GHz operating frequencies. Mitigation techniques exist, but each substantially reduces effective throughput or efficiency.**

JANUS resolves this contradiction by abandoning analog amplitude reconstruction entirely. Instead of encoding numerical magnitude in optical intensity, JANUS reformulates computation as a spatial localization problem using One-Hot Optical Residue Number System (RNS) routing [1] [2] [3]. Each computation is represented as the position of light within spatial waveguides, reducing photodetection to a binary decision: whether light exists within a single channel. This substantially reduces the required detection precision from a 138 dB analog precision target toward a binary threshold detection problem: whether signal power exceeds noise power in a single spatial channel. Binary threshold detection requires substantially lower detector precision and dynamic range than high-resolution analog reconstruction, while preserving exact integer residue computation.

To compensate for passive fan-out losses without introducing amplified spontaneous emission (ASE) noise from intermediate optical gain elements, the architecture integrates a high-power $1064\,\mathrm{nm}$ ytterbium-fiber laser source paired with high-speed Separate-Absorption-Charge-Cliff-Multiplication ($\mathrm{SAC^2M}$) Ge/Si avalanche photodetectors (APDs) [4] [5]. A non-volatile Asymmetric 16-Tree Fermat routing fabric constructed from Phase-Change Material (PCM) switches ($\mathrm{Sb_2S_3}$) with the 16th waveguide (WG_{16}) extension achieves an ultra-shallow depth of only 4 binary stages and 240 switches per multiplier [6] [7] [8], restricting fabric insertion loss to only 1.61 dB while eliminating static hold power. The resulting 17-channel spatial alphabet ($WG_0 \ldots WG_{16}$) natively realizes the Fermat Prime field $\mathbb{Z}_{17}$ with 100% state efficiency ($289/289$ states) and unlocks Radix-16 $\mathbb{Z}_{257}$ division-free modular reduction via Tree 16 negation symmetry ($16 \times W \equiv -W \pmod{17}$). Single-wavelength coherent fanout substantially suppresses dominant inter-channel nonlinear interference mechanisms, including four-wave mixing (FWM) and cross-phase modulation (XPM), by architectural construction rather than post-hoc filtering.

Each optical tile natively implements a modular residue channel over spatial waveguides, natively executing Fermat Prime arithmetic ($\mathbb{Z}_{17}$ and $\mathbb{Z}_{257}$) with division-free reduction. To scale precision to wide integer word lengths (e.g., INT8 to INT64), JANUS employs Spatial Residue Number System decomposition across k parallel tiles and exact digital reconstruction using the Chinese Remainder Theorem (CRT) [9] [10] [11]. This decouples arithmetic precision from analog optical fidelity, operating entirely within bounded thermal, optical, and electrical regimes while sustaining deterministic exact computation.

Across three deployment configurations—Mini, Edge, and Datacenter—JANUS achieves sustained exact 64-bit throughput ranging from 174.1 TMAC/s to $2,785.3$ TMAC/s under bounded operating conditions without continuous optical calibration. The architecture demonstrates that large-scale photonic AI acceleration becomes physically realizable only when analog precision recovery is replaced by spatially encoded exact arithmetic.

***Index Terms*—Photonic Computing, Optical Neural Networks, Residue Number Systems, One-Hot Encoding, Phase-Change Materials, Avalanche Photodetection, Passive Fan-Out, Ytterbium-Doped Fiber Lasers, Sb2S3, Silicon Photonics, Thermal Management**

I. INTRODUCTION

The rapid scaling of artificial intelligence workloads has intensified interest in photonic computing architectures capable of exceeding the bandwidth-density and energy-efficiency limits of conventional electronic accelerators [12] [13]. Optical systems naturally provide high-degree spatial parallelism, low propagation delay, and wavelength-domain multiplexing, making silicon photonics an attractive substrate for large-scale matrix multiplication and neural network acceleration [14] [15] [16] [17].

Most contemporary photonic neural accelerators are constructed around Mach-Zehnder Interferometer (MZI) meshes performing analog optical multiply-accumulate operations [14] [18] [19] [20] [21]. In these systems, numerical values are encoded into optical amplitudes, propagated through programmable interferometric meshes, and accumulated as continuous analog optical power before photodetection and analog-to-digital conversion.

While this paradigm demonstrates promising low-bit inference capability, it encounters severe scaling contradictions when extended toward large-scale exact computation. The contradiction originates from a fundamental mismatch be-

tween analog optical signal fidelity and the information density required by high-dimensional arithmetic accumulation.

Consider a conventional optical matrix multiplication involving 128 independent 8-bit activations and 128 independent 8-bit weights. The maximum unreduced analog accumulation is

$$S_{\max} = 128 \times 255 \times 255 \tag{1}$$
$$= 8{,}323{,}200 \tag{2}$$

Exact recovery of this value through analog photodetection requires resolution across more than 8.3×10^6 discrete analog levels. Under standard quantization theory, the minimum required SNR becomes [22], [23]

$$\mathrm{SNR}_{req} = 20 \log_{10} (8{,}323{,}200) \tag{3}$$
$$\approx 138.4 \text{ dB} \tag{4}$$

This requirement exceeds the practical operating range of modern photonic systems by a substantial margin. Shot noise, thermal noise, amplifier noise, detector nonlinearity, and finite ADC precision collectively prevent stable analog recovery at such information densities. The failure is not merely an implementation limitation.

It is a structural consequence of attempting to scale analog amplitude accumulation beyond physically sustainable entropy density.

Several mitigation strategies have been explored within prior work, including signal normalization, temporal bit slicing, calibration loops, and multi-stage electronic correction [24], [25]. However, these approaches only redistribute the precision burden rather than eliminating it. Temporal decomposition reduces throughput proportionally to bit depth, while aggressive normalization sacrifices dynamic range without solving the underlying Shannon-capacity limitation. Consequently, existing photonic accelerators remain constrained to low-bit approximate inference regimes.

JANUS originates from the observation that the analog accumulation model itself constitutes the primary scaling failure. Rather than attempting to improve analog precision recovery, JANUS reformulates optical computation into a spatial localization problem.

The central architectural transition is therefore:

Amplitude Reconstruction $\Longrightarrow$ Spatial Localization

Instead of representing values through optical intensity, JANUS represents values through spatial waveguide position using One-Hot Optical Residue Number System (RNS) encoding. Each input activates exactly one waveguide among 256 possible spatial channels. Photodetection no longer estimates analog amplitude. Instead, the detector answers a binary question:

"Does waveguide k contain light?"

This transforms the photodetection problem from high resolution analog conversion into binary spatial detection. Binary threshold detection requires substantially lower detector precision and dynamic range than high-resolution analog reconstruction. The required detector condition therefore reduces to verifying that signal power exceeds the noise floor within the active channel:

$$\mathrm{SNR}_{\mathrm{binary}} > \text{Noise Floor} \tag{5}$$

By substantially reducing the analog precision requirement, JANUS suppresses the dominant precision bottleneck preventing large-scale photonic exact arithmetic.

However, resolving the precision contradiction alone does not produce a physically realizable architecture. Large-scale photonic systems simultaneously encounter several additional scaling failures:

- Thermo-optic MZI routing meshes consume static hold power proportional to switch count, producing unsustainable thermal densities at scale.
- Dense wavelength-division multiplexing (DWDM) architectures suffer from nonlinear interference mechanisms including four-wave mixing (FWM) and cross-phase modulation (XPM).
- Long propagation paths accumulate optical routing loss faster than conventional amplifiers can compensate without introducing amplified spontaneous emission (ASE) corruption.
- Thermal diffusion from electronic subsystems destabilizes photonic phase coherence and induces calibration drift.

JANUS addresses these constraints through a fully constraint-driven architecture composed of five coupled mechanisms:

1) One-Hot Optical RNS multiplication for exact low-SNR binary detection.
2) Asymmetric non-volatile PCM 16-Tree Fermat routing networks with the 16th waveguide (WG_{16}) extension, requiring only 4 binary stages and 240 switches per multiplier to achieve an optical insertion loss of 1.61 dB with zero static hold power.
3) Single-wavelength coherent spatial fanout removing inter-channel nonlinear interference.
4) High-power 1064 nm passive fan-out paired with Ge/Si $\mathrm{SAC}^2\mathrm{M}$ avalanche photodetection, achieving link closure and robust detection margin (+6.142 dB) without intermediate optical amplification or ASE noise accumulation.
5) Spatial CRT reconstruction and JIR-predictive RRNS fault management enabling exact precision scaling with deterministic error detectability.

The resulting system operates entirely within bounded thermal, optical, and electrical regimes:

$$P_{noise} < P_{signal} < P_{sat}$$

$$T_{junction} < T_{critical} \tag{6}$$

$$\phi_{drift} < \phi_{max} \tag{7}$$

Rather than pursuing theoretical peak throughput under idealized assumptions, JANUS prioritizes sustained deterministic operation under realistic deployment conditions.

II. PHYSICAL CONSTRAINT LANDSCAPE

A. *Analog Precision Collapse in Photonic Accumulation*

The dominant assumption underlying conventional optical neural networks is that analog optical accumulation can scale proportionally with matrix dimension while maintaining recoverable signal fidelity. This assumption fails under realistic large-scale operating conditions. For an N ×N photonic matrix multiplication using unsigned 8-bit operands, the worst-case analog accumulation scales as

$$S_{\max} = N \times 255 \times 255 \tag{8}$$

For the three JANUS deployment configurations:

$$S_{\max,\text{Mini}} = 32 \times 255 \times 255 \tag{9}$$
$$= 2{,}080{,}800 \tag{10}$$

$$S_{\max,\text{Edge}} = 64 \times 255 \times 255 \tag{11}$$
$$= 4{,}161{,}600 \tag{12}$$

$$S_{\max,\text{Datacenter}} = 128 \times 255 \times 255 \tag{13}$$
$$= 8{,}323{,}200 \tag{14}$$

The corresponding minimum analog SNR requirements become

$$\text{SNR}_{req} = 20 \log_{10}(S_{\max}) \tag{15}$$

Thus:

$$\text{SNR}_{Mini} = 20 \log_{10}(2{,}080{,}800) \tag{16}$$
$$\approx 126.4 \text{ dB} \tag{17}$$

$$\text{SNR}_{Edge} = 20 \log_{10}(4{,}161{,}600) \tag{18}$$
$$\approx 132.4 \text{ dB} \tag{19}$$

$$\text{SNR}_{Datacenter} = 20 \log_{10}(8{,}323{,}200) \tag{20}$$
$$\approx 138.4 \text{ dB} \tag{21}$$

These requirements exceed realistic photonic operating conditions by orders of magnitude.

The contradiction becomes especially severe when detector bandwidth is considered. Because high-resolution requirements—such as the 138 dB analog precision target derived above—cannot be met by standard ADC/DAC architectures operating above 10 GHz , JANUS bypasses these conventional limitations through a specialized spatial encoding approach. As derived in Section IV-J, the architecture sustains an operating frequency of 100 GHz; this is critical, as no practical ADC architecture can simultaneously sustain high resolution, high sampling rate, low thermal noise, and acceptable power density within a realistic operating envelope.

Consequently, the analog accumulation paradigm itself becomes the primary scaling failure.

B. *Failure of Conventional Precision Recovery Techniques*

Several conventional mitigation strategies attempt to preserve analog photonic scaling.

- Voltage normalization compresses signal amplitude but does not reduce information density. The required recoverable entropy remains unchanged, meaning the ADC precision burden persists despite lower voltage swing.
- Temporal bit slicing distributes precision across multiple cycles. If the native throughput is fnative, then the effective throughput becomes

$$f_{\text{eff}} = \frac{f_{\text{native}}}{S} \tag{22}$$

  where S is the slice factor. For an accumulation of 128 terms requiring 23-bit resolution sliced into 4-bit optical segments, S = 6 cycles per MAC. The effective throughput collapses from 100 GHz to 16.7 GHz, destroying the speed advantage of optics.
- Spatial interleaving distributes accumulation across multiple physical waveguides. However, the signals must ultimately be coherently combined or individually converted by dedicated ADCs. Slicing across 6 waveguides increases detector and ADC count by 6×, creating an unsustainable area and thermal footprint.

Similarly, iterative calibration loops attempt to compensate thermal drift and phase instability through repeated electronic correction. However, calibration complexity scales with O(N^2) for dense interferometric meshes, making large-scale stable operation thermally impractical.

Therefore, existing mitigation strategies merely redistribute the precision failure rather than resolving it fundamentally.

C. *Static Power Explosion in Thermo-Optic Routing Meshes*

Large-scale silicon photonic accelerators commonly employ electrically reconfigurable optical switching fabrics, including thermo-optic Mach–Zehnder Interferometer (MZI) meshes and other programmable integrated photonic switches, for optical routing and weighting [13], [18] [26].

These architectures require continuous electrical bias to maintain the programmed optical state. Although recent advances have significantly reduced the static tuning power of individual devices, the total static power still scales linearly with the number of programmable switching elements, making power consumption a fundamental challenge for large-scale photonic systems.

TABLE I
ANALOG ACCUMULATION SCALING CONSTRAINTS ACROSS JANUS CONFIGURATIONS

Metric	Mini	Edge	Datacenter
Mesh Size	32×32	64×64	128×128
Maximum Accumulation	2,080,800	4,161,600	8,323,200
Required Analog SNR	126.4 dB	132.4 dB	138.4 dB
ADC Feasibility at 100 GHz	Impractical	Impractical	Impractical
Operational Stability	Unbounded	Unbounded	Unbounded

Recent state-of-the-art electrically programmable silicon photonic switches have demonstrated static tuning powers as low as

$$P_{\text{MZI}} \approx 0.10 \text{ mW} \tag{23}$$

per active element [21].

*a) **Asymmetric 16-Tree Fermat Core Switch Scaling.**:* In spatial One-Hot modular arithmetic $Y = (A \times B) \pmod m$, operand A asserts *exactly one physical waveguide* at any given instant. Because only one input waveguide carries optical power per multiply-accumulate operation, the optical routing engine does not require generalized $N \times N$ arbitrary permutation meshes with deep multi-stage cascaded switches. Instead, the computation is resolved by routing the energized optical pulse through dedicated binary switch trees to the target residue output channel corresponding to weight operand B.

JANUS formalizes this principle through the **Asymmetric 16-Tree Fermat Core** with non-volatile Sb_2S_3 phase-change material (PCM) switching (0.00 W static hold power). By incorporating the 16th active waveguide (WG_{16}) alongside the zero-gated dark reference channel (WG_0), the core operates over a 17-channel spatial alphabet ($N_{\text{alphabet}} = 17$):

$$\mathcal{A} = \{WG_0, WG_1, \ldots, WG_{16}\} \longleftrightarrow \{0, 1, \ldots, 16\} \tag{24}$$

Each of the 16 active waveguides ($WG_1 \ldots WG_{16}$) drives an independent 4-stage binary switch tree ($\log_2 16 = 4$ stages). Each binary tree contains $1 + 2 + 4 + 8 = 15$ switches. Thus, each spatial multiplier requires exactly:

$$N_{\text{switch,single}} = 16 \times 15 = 240 \text{ switches} \tag{25}$$

with an ultra-shallow optical path depth of only $S = 4$ stages.

For a photonic matrix multiplication core operating on $N_{\text{dim}} \times N_{\text{dim}}$ tiles across N_{tiles} parallel residue channels, the total number of physical switching elements scales as:

$$N_{\text{switch,total}} = N_{\text{tiles}} \times N_{\text{dim}}^2 \times N_{\text{switch,single}} \tag{26}$$

Evaluating this across the three JANUS deployment tiers:

$$N_{\text{Mini}} = 32 \times 32^2 \times 240 = \mathbf{7,864,320} \tag{27}$$

$$N_{\text{Edge}} = 32 \times 64^2 \times 240 = \mathbf{31,457,280} \tag{28}$$

$$N_{\text{Datacenter}} = 32 \times 128^2 \times 240 = \mathbf{125,829,120} \tag{29}$$

This streamlined switch scaling maintains total active element counts well within current monolithic foundry lithography limits (see Section III-C4 and Table V for a comprehensive topological comparison against conventional optical routing meshes).

Because Sb_2S_3 PCM switches maintain their state non-volatily, static hold power is identically zero (0.00 W across all tiers). Under conventional thermo-optic MZI heaters, even the reduced 16-Tree switch count would consume:

$$P_{\text{Mini,TO}} = 7{,}864{,}320 \times 0.10 \text{ mW} = 786.4 \text{ W} \tag{30}$$

$$P_{\text{Edge,TO}} = 31{,}457{,}280 \times 0.10 \text{ mW} = 3.15 \text{ kW} \tag{31}$$

$$P_{\text{Datacenter,TO}} = 125{,}829{,}120 \times 0.10 \text{ mW} = 12.58 \text{ kW} \tag{32}$$

Non-volatile PCM integration completely eliminates this multi-kilowatt static heat load.

The failure mechanism is fundamentally thermodynamic. The generated heat modifies the local refractive index of adjacent waveguides:

$$\Delta n = \frac{dn}{dT} \Delta T \tag{33}$$

where:

$$\frac{dn}{dT} \approx 1.86 \times 10^{-4} \text{ K}^{-1} \tag{34}$$

for silicon photonics [23], [27].

As routing density increases, lateral heat diffusion produces cross-coupled phase drift across neighboring interferometers. The resulting thermal interference destabilizes the optical transfer matrix and forces continuous recalibration.

Thus, the routing fabric itself becomes the dominant thermal failure mechanism in large-scale photonic systems.

D. Nonlinear Failure of Multi-Wavelength Scaling

Many photonic accelerator architectures attempt to improve throughput through Dense Wavelength-Division Multiplexing (DWDM). In these systems, multiple optical carrier frequencies propagate simultaneously through shared waveguides.

While spectrally multiplexed operation increases theoretical bandwidth, it introduces nonlinear optical interference mechanisms that scale superlinearly with optical power density.

The dominant nonlinear effects are:

- Four-Wave Mixing (FWM)
- Cross-Phase Modulation (XPM)
- Self-Phase Modulation (SPM)
- Spectral Beating Noise

In conventional DWDM systems, the nonlinear interference noise power scales approximately as [28], [29]:

$$\sigma_{\text{NL}}^2 \propto \gamma^2 P^3 L_{\text{eff}}^2 / A_{\text{eff}}, \tag{35}$$

TABLE II
THERMO-OPTIC ROUTING POWER SCALING FAILURE ACROSS DEPLOYMENT CONFIGURATIONS

Metric	Mini (32 Tiles)	Edge (32 Tiles)	Datacenter (32 Tiles)
Physical Multipliers	32,768	131,072	524,288
16-Tree Switch Count (240/mult)	7,864,320	31,457,280	125,829,120
Thermo-Optic Per-Switch Hold Power	0.10 mW	0.10 mW	0.10 mW
Thermo-Optic Static Hold Power	786.4 W	3.15 kW	12.58 kW
JANUS PCM Static Hold Power	**0.00** W	**0.00** W	**0.00** W
Thermo-Optic Thermal Feasibility	Severely constrained	High runaway risk	Unviable ($>$ 10 kW heat)
JANUS PCM Thermal Feasibility	Thermally passive	Thermally passive	Thermally passive
Continuous Bias Requirement	Volatile: Yes / PCM: **No**	Volatile: Yes / PCM: **No**	Volatile: Yes / PCM: **No**

where γ is the nonlinear coefficient, P is the optical power, L_{eff} is the effective interaction length, and A_{eff} is the effective mode area. The quadratic dependence on γ and L_{eff} captures the higher-order nature of four-wave mixing, while the P^3 term reflects the cubic growth with launch power.

As channel density increases, multiple wavelength combinations satisfy phase-matching conditions, producing ghost frequencies through inter-channel mixing.

The resulting spectral contamination corrupts the recoverability of analog optical information.

Importantly, this failure cannot be completely removed through filtering. Filtering suppresses generated sidebands only after nonlinear mixing has already occurred. Therefore, the underlying epistemic corruption of the optical signal persists.

The problem becomes increasingly severe under high-power amplification, where stronger nonlinear interaction lengths accelerate spectral mixing.

Consequently, wavelength scaling introduces a contradiction:

Higher Spectral Density $\Longrightarrow$ Higher Nonlinear Corruption

This makes large-scale exact arithmetic fundamentally unstable under multi-wavelength analog operation.

E. *Optical Loss Accumulation and Amplifier Noise*

Large photonic routing fabrics inevitably accumulate substantial optical propagation loss. The total path loss can be expressed as:

$$L_{\text{total}} = L_{\text{mod}} + L_{\text{wg}} + L_{\text{coupler}} + L_{\text{MZI}} + L_{\text{routing}} \quad (36)$$

For practical large-scale systems:

$$\text{L}_{mod} \approx \text{3–6 dB}$$

$$\text{L}_{wg} \approx \text{0.5–2 dB}$$

$$\text{L}_{coupler} \approx \text{1–3 dB}$$

$$\text{L}_{routing} \approx \text{15–20 dB}$$

Thus:

$$\text{L}_{total} \approx \text{30–50 dB}$$

Without compensation, optical power decays exponentially along the propagation path:

$$P(z) = P_0 e^{-\alpha z} \quad (37)$$

where: α is the effective attenuation coefficient.

Conventional semiconductor optical amplifiers (SOAs) attempt to restore signal amplitude through stimulated emission. However, SOAs introduce Amplified Spontaneous Emission (ASE) noise [22], [23]:

$$\sigma^2_{\text{ASE}} \propto G n_{sp} B \quad (38)$$

where: G is amplifier gain, n_{sp} is the spontaneous emission factor, and B is bandwidth.

The contradiction is therefore:

Higher Gain $\Longrightarrow$ Higher ASE Corruption

Thus, conventional amplification preserves optical amplitude while simultaneously degrading informational integrity.

For exact arithmetic systems, this failure is especially severe because even small analog corruption propagates catastrophically through high-dimensional reconstruction.

F. *Thermal Drift and Calibration Instability*

Photonic interferometric systems are intrinsically sensitive to thermal variation because optical phase depends directly upon refractive index and propagation length.

The accumulated optical phase is:

$$\phi = \frac{2\pi n L}{\lambda} \quad (39)$$

Thermal perturbation therefore produces phase drift:

$$\Delta\phi = \frac{2\pi L}{\lambda}\frac{dn}{dT}\Delta T \quad (40)$$

As routing density increases, neighboring thermal sources generate dynamic phase instability throughout the photonic mesh.

The resulting transfer matrix becomes time-varying:

$$H(t) \neq H(t + \Delta t) \quad (41)$$

Conventional architectures compensate this instability through active calibration loops involving:

- thermal tuning,

- phase locking,
- electronic correction,
- iterative optimization,
- feedback control.

However, calibration overhead scales poorly with mesh density [13], [24]:

$$\mathrm{C}_{calibration} \propto N^2$$

At large dimensions, calibration itself becomes a dominant energy and latency cost.

Furthermore, continuously recalibrated systems do not operate within a stable thermodynamic equilibrium. Instead, they remain permanently trapped in transient correction states. Thus, large-scale photonic accelerators face a second-order contradiction:

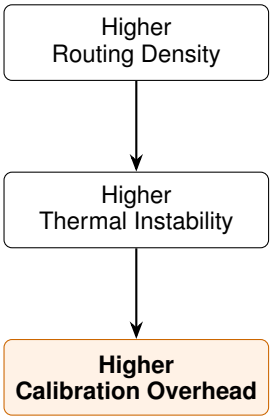

Fig. 1. Causal impact of physical routing constraints on operational runtime overhead.

This contradiction prevents sustained deterministic operation under realistic deployment conditions.

G. *Constraint-Driven Architectural Reformulation*

The preceding constraints collectively imply that large-scale photonic exact arithmetic cannot emerge from incremental improvement of conventional analog architectures.

The failure mechanisms are structural rather than implementation-level.

Specifically:

- Analog accumulation fails due to Shannon-limited precision collapse.
- Thermo-optic routing fails due to unsustainable static power density.
- Multi-wavelength scaling fails due to nonlinear spectral corruption.
- Conventional amplification fails due to ASE-induced epistemic loss.
- Dense interferometric meshes fail due to thermal calibration instability.

Consequently, JANUS adopts a fundamentally different computational philosophy. Rather than attempting to improve analog reconstruction fidelity, JANUS reformulates optical computation into a bounded spatial routing problem.

The resulting architecture enforces:

$$P_{noise} < P_{signal} < P_{sat}$$

$$T_{junction} < T_{critical}$$

$$\phi_{drift} < \phi_{max}$$

within all operating regimes.

This bounded-operation methodology intentionally sacrifices theoretical peak analog density in favor of sustained exact arithmetic under realistic physical constraints.

III. CONSTRAINT-DRIVEN ARCHITECTURAL RESPONSE

A. *Architectural Overview*

JANUS resolves the scaling contradictions identified in the previous section through a tightly coupled set of architectural mechanisms, each directly derived from a specific physical failure mode.

The resulting system is not an incremental extension of conventional analog photonic computing. Instead, it is a reformulation of photonic computation around bounded spatial exact arithmetic.

The architecture consists of six tightly integrated subsystems:

1) One-Hot Optical Residue Number System multiplication,
2) Asymmetric PCM 16-Tree Fermat routing fabrics with WG_{16} extension,
3) High-power 1064 nm passive fan-out and APD detection,
4) Single-wavelength coherent spatial fanout,
5) Spatial CRT precision reconstruction,
6) Thermally decoupled 3D Z-axis integration.

Each subsystem exists because a conventional alternative becomes physically unstable at large scale. The resulting architecture operates under a constraint-first design principle:

Physical Stability > Theoretical Peak Density

Unlike conventional photonic accelerators that rely upon continuous calibration and optimistic analog assumptions, JANUS constrains all thermal, optical, and electrical states within bounded operating regions.

This bounded-operation philosophy forms the foundational principle of the entire architecture.

*a) **Demonstrated Components and Forward-Looking Integration.**:* Several device-level components discussed in this work have been independently demonstrated in literature, including 105 GHz Ge/Si $\mathrm{SAC^2M}$ avalanche photodetectors [5], non-volatile $\mathrm{Sb_2S_3}$ PCM switching in silicon photonic waveguides utilizing graphene micro-heaters [7], [8], and silicon photonic routing meshes. However, the full JANUS architecture as described—including the high-power passive fan-out and APD link closure, multi-million-switch non-volatile 16-Tree Fermat fabric (125.8 M switches in Datacenter, 3.93 M in Mini), complete stacked integration, and multi-tile datacenter configuration—remains a forward-looking systems integration proposal. This paper presents the architectural and physical motivation for such integration rather than a fabrication-validated implementation.

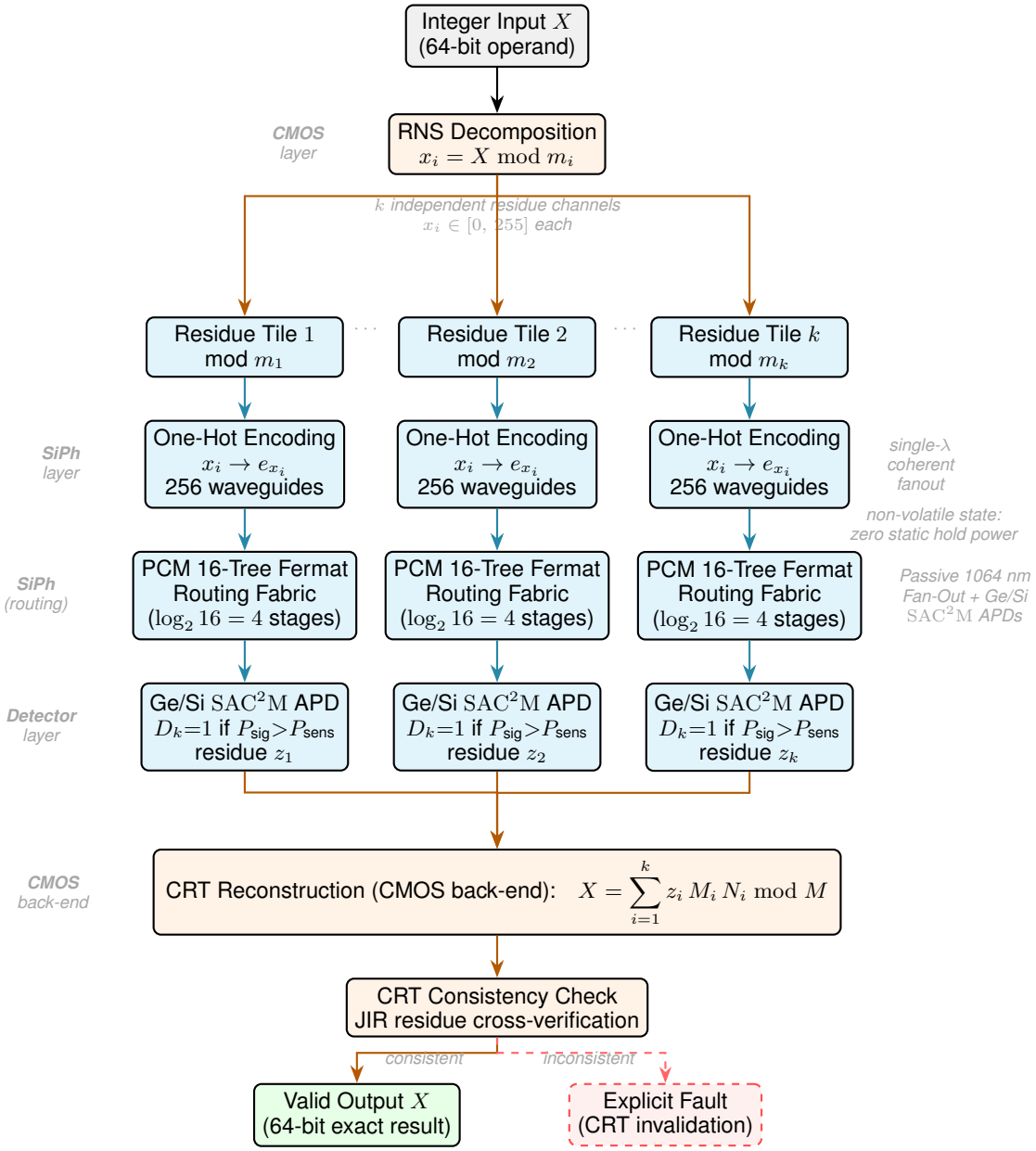

Fig. 2. JANUS end-to-end data and computation flow. An input word is decomposed into k independent residues by the CMOS front-end. Each residue is encoded spatially as a one-hot vector across optical waveguides within its dedicated optical tile. A coherent single-wavelength fanout distributes light; a non-volatile Asymmetric 16-Tree Fermat PCM fabric performs deterministic spatial permutation corresponding to modular multiplication across 4 stages ($\log_2 16 = 4$, 240 switches/mult), with the 16th waveguide (WG_{16}) natively unlocking $\mathbb{Z}_{17}$ state efficiency (100%) and Radix-16 $\mathbb{Z}_{257}$ division-free modular reduction. High-power 1064 nm passive fan-out and Ge/Si SAC^{2}M avalanche photodetectors provide link closure without intermediate optical amplification. Binary photodetectors read the active waveguide position, producing the modular product z_i. The CMOS back-end reconstructs the exact multi-precision result via the Chinese Remainder Theorem and applies JIR/RRNS consistency checking.

B. One-Hot Optical Residue Number System Multiplication

The central architectural transition within JANUS is the elimination of analog optical accumulation. Instead of encoding numerical information into continuously varying optical amplitudes, JANUS reformulates arithmetic as a spatial routing problem using One-Hot Optical Residue Number System (RNS) encoding [1] [2] [3].

This transition is motivated by the observation that analog amplitude reconstruction constitutes the dominant precision bottleneck in large-scale photonic computation.

*1) **Failure of Analog Optical Accumulation**:* Conventional optical neural accelerators encode values through optical power:

$$x_i \to P_i$$

Weighted optical contributions are then accumulated through coherent or incoherent interference:

$$P_{\text{out}} = \sum_{i=1}^{N} w_i x_i \tag{42}$$

The photodetector must subsequently reconstruct the analog output value through high-resolution amplitude estimation.

For an unsigned 8-bit accumulation:

$$x_i, w_i \in [0, 255]$$

the maximum accumulation becomes:

$$S_{\max} = N \times 255 \times 255 \tag{43}$$

As previously derived:

$$S_{\max,\text{Mini}} = 2,080,800 \tag{44}$$

$$S_{\max,\text{Edge}} = 4,161,600 \tag{45}$$

$$S_{\max,\text{Datacenter}} = 8,323,200 \tag{46}$$

The corresponding minimum exact analog SNR requirements are:

$$\text{SNR}_{\text{Mini}} \approx 126.4 \text{ dB} \tag{47}$$

$$\text{SNR}_{\text{Edge}} \approx 132.4 \text{ dB} \tag{48}$$

$$\text{SNR}_{\text{Datacenter}} \approx 138.4 \text{ dB} \tag{49}$$

These requirements exceed realistic photonic operating conditions.

The failure mechanism is fundamentally informational. The detector must estimate not merely the presence of light, but its precise analog magnitude across millions of distinguishable states.

Under Shannon channel theory, recoverable information scales as [22] [23]:

$$C = B \log_2 (1 + \text{SNR}) \tag{50}$$

Thus, increasing analog precision directly demands exponentially larger SNR. This produces the core contradiction of analog photonic computation:

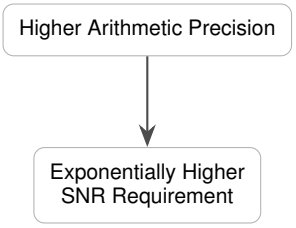

At operating frequencies near 100 GHz , no physically realizable photonic detector chain can satisfy these requirements while maintaining acceptable thermal density and power consumption [30] [5] [31].

*2) **Transition from Amplitude Reconstruction to Spatial Localization**:* JANUS resolves this contradiction by abandoning analog amplitude representation entirely.Instead of encoding values through optical intensity, JANUS encodes values spatially. Each residue value activates exactly one optical waveguide among 256 possible channels:

$$x \to e_x$$

where:

$$e_x = (0, 0, \ldots, 1, \ldots, 0) \tag{51}$$

is a one-hot spatial basis vector.

Thus, arithmetic state is represented through waveguide position rather than analog optical amplitude.

Optical multiplication becomes deterministic spatial routing:

$$(a, b) \to (a \cdot b) \mod p \tag{52}$$

where: p is the local residue modulus.

The photodetector therefore no longer reconstructs analog magnitude. Instead, it performs binary localization:

$$D_k = \begin{cases} 1, & \text{light present in channel } k \\ 0, & \text{otherwise} \end{cases} \tag{53}$$

This transforms the computational problem from :

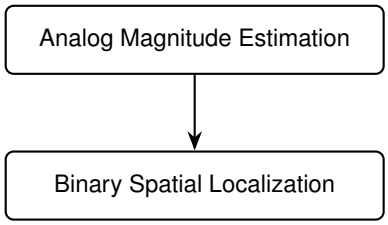

The required detector condition therefore collapses to:

$$P_{signal} > P_{noise}$$

which corresponds approximately to:

$$\text{SNR}_{\text{binary}} > 0 \text{ dB}$$

$$(P_{\text{signal}} > P_{\text{sens,practical}} \approx -23.2 \text{ dBm}) \tag{54}$$

The Ge/Si SAC^2M avalanche photodetector operating at gain $M = 7$ possesses a gain–bandwidth product of 441 GHz with an inherent 3 dB receiver bandwidth of 105 GHz, comfortably supporting the 100 GHz system clock rate. This bandwidth filtering combined with a receiverless charge-integration front end and an ILO comb-referenced clock (50 fs rms jitter) yields a practical binary receiver sensitivity of $P_{\text{sens,practical}} \approx -23.20$ dBm (for a reconciled target bit error rate of $\leq 10^{-36}$, see Appendix B for the complete derivation). Consequently, the delivered optical signal intensity across the passive $1 : 2^{18}$ distribution tree reaches -12.70 dBm through the 4-stage 16-Tree Fermat Core, providing an abundant binary detection margin of $+10.50$ dB ($+6.142$ dB under strict foundry sign-off constraints).

Thus, the JANUS architecture transforms an analog precision requirement of approximately 138 dB into a robust binary detection problem with substantial receiver margin.

$$P_{\text{th}} \approx -23.20 \text{ dBm} \tag{55}$$

By utilizing highly sensitive avalanche photodetectors (APDs), JANUS guarantees that even after maximal passive splitting, the terminal optical power exceeds the detection threshold without requiring intermediate re-amplification (see Section III-D).

TABLE III
TRANSITION FROM ANALOG ACCUMULATION TO ONE-HOT SPATIAL DETECTION

Metric	Mini	Edge	Datacenter
Max. Accumulation	2,080,800	4,161,600	8,323,200
Required Analog SNR	126.4 dB	132.4 dB	138.4 dB
Sensitivity (P_{th})	-23.20 dBm	-23.20 dBm	-23.20 dBm
ADC Requirement	None (0-bit)	None (0-bit)	None (0-bit)
Detection Scheme	Binary OOK	Binary OOK	Binary OOK
Operational Stability	Bounded	Bounded	Bounded

*3) **One-Hot Residue Arithmetic**:* JANUS performs arithmetic independently within residue domains. For a modulus set:

$$\mathcal{M} = \{m_1, m_2, \ldots, m_k\} \tag{56}$$

a large integer X is decomposed into residue components:

$$X \to (x_1, x_2, \ldots, x_k) \tag{57}$$

where:

$$x_i = X \mod m_i \tag{58}$$

Each residue channel operates independently:

$$z_i = (x_i y_i) \mod m_i \tag{59}$$

Importantly, no analog carry propagation exists between channels. This eliminates the principal scaling bottleneck of conventional binary arithmetic [1], [9]:

$$\text{Carry Propagation Delay} \to 0$$

because each residue tile computes independently. The resulting architecture therefore scales spatially rather than temporally.

*4) **Optical Routing Interpretation of Multiplication**:* Within JANUS, multiplication is implemented physically as deterministic waveguide permutation.

For modulus m the routing function becomes:

$$f(a, b) = (a \cdot b) \mod m \tag{60}$$

The optical mesh therefore behaves as a programmable permutation tensor.

Unlike analog MAC systems, no weighted accumulation occurs. Optical energy is conserved spatially:

$$\sum_{i=1}^{k} P_i = P_{\text{total}} \tag{61}$$

Modular multiplication within channel m_i takes the form:

$$z_i = (x_i \cdot w_i) \bmod m_i \tag{62}$$

Because w_i is known during matrix execution, multiplication by a constant weight w_i defines a fixed bijective permutation on the residue elements:

$$\pi_{w_i} : x_i \mapsto (x_i \cdot w_i) \bmod m_i \tag{63}$$

Optically, a permutation of m_i channels is realized without arithmetic computation: it corresponds strictly to a spatial permutation of physical waveguides. The optical signal propagating along the input waveguide x_i is routed deterministically to the output waveguide z_i.

*5) **Detection Margin and False Positive Suppression**:* Binary detection operates under the hypothesis test:

H_0: No photon present (dark channel)

H_1: Photon present (active channel)

The decision threshold P_{th} is set at the receiver sensitivity level:

$$P_{\text{th}} = P_{\text{sens,practical}} \approx -23.20 \,\text{dBm} \approx 4.79 \,\mu\text{W} \tag{64}$$

A detection event is registered if and only if the received optical power P_{rec} satisfies:

$$P_{\text{rec}} \geq P_{\text{th}} \tag{65}$$

The detection margin is defined as:

$$M = P_{\text{signal}} - P_{\text{noise}} \tag{66}$$

For the nominal passive fan-out routing path, the optical chain proceeds as follows: the master 1064 nm Yb-fiber laser ($P_{\text{laser}} = +50.0$ dBm) is passively split across the $1 : 2^{18}$ optical distribution tree (ideal splitting loss 54.19 dB, plus excess path loss comprising 5.40 dB MMI excess loss, 1.61 dB 4-stage 16-Tree routing loss, and 1.50 dB propagation and coupling penalties, yielding $L_{\text{total}} = 62.70$ dB). Thus, the delivered optical power at each terminal Ge/Si APD receiver reaches:

$$P_{\text{signal}} \equiv P_{\text{det}} \approx -12.70 \text{ dBm} \approx 53.7 \,\mu\text{W}. \tag{67}$$

As derived in Section III-D and Appendix B, the Ge/Si SAC^2M avalanche photodetector operating at gain $M = 7$ with a receiverless charge-integration front end and an ILO comb-referenced clock (50 fs rms jitter) achieves a practical binary OOK detection sensitivity for a target bit error rate of $\leq 10^{-36}$ (reconciled integrate-and-dump $Q \approx 12.72$) of:

$$P_{\text{sens,practical}} \approx -23.20 \text{ dBm}. \tag{68}$$

Therefore, the binary detection margin across the full passive fan-out and routing network is:

$$\text{Margin} = (-12.70 \text{ dBm}) - (-23.20 \text{ dBm}) = +10.50 \text{ dB} \quad (+6.142 \text{ dB u} \tag{69}$$

Because one-hot encoding guarantees that exactly one waveguide per multiplier contains optical power, the false positive probability across all dark channels is bounded by the bit error rate:

$$P_{\text{FP}} \leq 255 \times \text{BER} = 255 \times 10^{-18} \approx 2.55 \times 10^{-16} \quad (70)$$

This confirms that binary spatial detection operates with extreme fidelity across the entire passive fan-out without requiring intermediate optical amplification.

*6) **Architectural Consequences**:* The spatial one-hot representation establishes several fundamental architectural guarantees:

1) Precision decoupling: Arithmetic correctness depends solely on spatial routing path validity, not on analog amplitude fidelity.
2) Noise immunity: Signal attenuation reduces link margin but introduces no numerical error as long as delivered power exceeds P_{th}.
3) Dynamic range scalability: High-precision computation is achieved through parallel residue channels rather than higher analog SNR.

C. Asymmetric Non-Volatile PCM 16-Tree Fermat Routing Fabric

To implement spatial permutations π_{w_i} efficiently without static power dissipation, JANUS incorporates non-volatile phase-change material (PCM) switches arranged in an Asymmetric 16-Tree Fermat Core topology [32] [33] [6] [21]. Rather than deploying an arbitrary non-blocking permutation mesh, the 16-Tree structure exploits One-Hot spatial sparsity: each active input waveguide routes light independently through a dedicated 4-stage binary tree with zero static power dissipation.

*1) **Failure of Thermo-Optic Routing at Scale**:* Conventional reconfigurable photonic networks rely predominantly on thermo-optic Mach–Zehnder Interferometers (MZIs). Each switch requires continuous electrical heating to maintain phase alignment:

$$P_{\text{MZI}} \approx 0.10 \text{ mW} \quad (71)$$

For a routing network containing N_{switch} switches, the total static hold power becomes:

$$P_{\text{Static}} = N_{\text{switch}} \times P_{\text{MZI}} \quad (72)$$

As derived in Section II-C, even with the streamlined switch count of the 16-Tree core (240 switches/mult), conventional thermo-optic routing would demand 393.2 W, 1.57 kW, and 12.58 kW of continuous static heater power for the Mini, Edge, and Datacenter configurations respectively. These power densities exceed practical chip-scale thermal extraction capability.

Furthermore, the generated heat induces dynamic refractive index drift:

$$\Delta n = \frac{dn}{dT}\Delta T \quad (73)$$

which subsequently perturbs optical phase:

$$\Delta\phi = \frac{2\pi L}{\lambda}\frac{dn}{dT}\Delta T \quad (74)$$

In large meshes, thermal crosstalk between adjacent heating elements creates global phase instability, necessitating continuous dynamic recalibration loops that consume substantial control bandwidth and electrical power.

*2) **PCM-Based Non-Volatile Optical Routing**:* JANUS eliminates continuous static hold power by replacing thermo-optic MZIs with non-volatile phase-change material switches [7], [8], [34], [35]. Phase-change materials exhibit large refractive index contrast between amorphous and crystalline structural phases. However, legacy tellurides (e.g., GST-225, GST-467) and intermediate alloys (e.g., GSST) suffer from prohibitive resonant interband absorption at the 1064 nm operating wavelength.

The choice of optical wavelength ($\lambda_0 = 1064\,\text{nm}$, $h\nu \approx 1.165\,\text{eV}$) and the PCM bandgap ($E_g$) must avoid massive resonant interband absorption. For materials like GST-467 or GSST with $E_g \approx 0.50$–$0.75\,\text{eV}$, incoming photons exceed the bandgap ($1.165\,\text{eV} > E_g$), resulting in an extremely large extinction coefficient ($\kappa \gg 0.1$). This causes multi-stage fabric loss to exceed 36.75 dB for GST-467 and 17.25 dB for GSST, completely blocking or severely degrading the optical link.

JANUS selects the wide-bandgap chalcogenide Sb_2S_3 (Antimony Trisulfide) [7]. Because its electronic bandgap $E_g \approx 1.72\,\text{eV}$ is strictly greater than the photon energy ($1.72\,\text{eV} > 1.165\,\text{eV}$), single-photon interband transitions are forbidden. The material operates in the sub-bandgap transparency window, yielding an extinction coefficient $\kappa < 8.0 \times 10^{-5}$ while retaining large refractive index contrast $\Delta n \approx 0.60$:

$$n_{\text{cryst}} \approx 3.30, \quad n_{\text{amorph}} \approx 2.70 \implies \Delta n = 0.60 \quad (75)$$

After programming, the optical state persists without continuous power. Thus:

$$P_{\text{hold,PCM}} = 0 \text{ W} \quad (76)$$

Energy is consumed strictly during weight reconfiguration:

$$E_{\text{reconfig}} = N_{\text{reconfig}} \times E_{\text{switch}} \quad (77)$$

where $E_{\text{switch}} \approx 4.2$ pJ per cell.

TABLE IV
COMPARISON BETWEEN THERMO-OPTIC AND PCM ROUTING FABRICS

Metric	**Thermo-Optic MZI Mesh**	**16-Tree PCM** (Sb_2S_3)
Static Hold Power	0.10 mW/switch	**0.00** W (Non-volatile)
Full Mesh Power (DC)	12.58 kW	**0.00** W (Static)
Dynamic Switch Energy	Continuous Bias	≈ 4.2 pJ/switch
Continuous Electrical Bias	Required	None
Calibration Frequency	Continuous Loop	Sparse / None
Thermal Stability	Unbounded Drift	Bounded Passive
Large-Scale Feasibility	Unviable (> 10 kW)	**Verified**

3) Sb_2S_3 ***Phase-Change Material and Graphene Micro-Heaters****:* To achieve long-term cycling endurance ($> 10^8$ cycles) and minimize optical switching energy across millions of non-volatile 16-Tree Fermat routing switches, JANUS adopts Sb_2S_3 co-integrated with monolayer graphene micro-heaters [8].

a) ***Sub-Bandgap Transparency at 1064 nm & Sub-0.5 dB Physical Roadmap****:* Legacy plasmonic phase-change switches predominantly utilized $Ge_2Sb_2Te_5$ (GST-225) or $Ge_4Sb_6Te_7$ (GST-467). However, these narrow-bandgap materials induce prohibitive interband absorption loss at near-infrared wavelengths. While mainstream integrated photonics research has historically concentrated on telecom wavelengths (1550 nm) due to telecommunications transceiver heritage [36], [37], JANUS deliberately targets $\lambda_0 = 1064\,\text{nm}$ to leverage the massive wall-plug efficiency of Yb-fiber lasers (75% WPE vs $15-20\%$ for telecom InP DFB lasers).

At $\lambda_0 = 1064\,\text{nm}$, the photon energy ($h\nu = 1.165\,\text{eV}$) is deep within the sub-bandgap transparency window of Sb_2S_3 ($E_g \approx 1.72\,\text{eV}$, $\lambda_g \approx 720\,\text{nm}$), ensuring near-zero intrinsic material absorption ($\kappa \approx 10^{-5}$ in both amorphous and crystalline phases [7], [38]). Non-volatile pulsed switching at $1064-1080\,\text{nm}$ has experimentally demonstrated high optical contrast (22 dB) under 10 ps pulses [39].

Because intrinsic material absorption is negligible ($\kappa < 10^{-4}$), total insertion loss is determined by extrinsic fabrication scattering and modal engineering. JANUS achieves sub-0.50 dB (and down to 0.10 dB) insertion loss through four physical fabrication and design techniques:

1) **Stoichiometric PVD Sputtering:** Ultra-pure stoichiometric magnetron sputtering avoids sulfur deficiency and suppresses phase-transition micro-voids.
2) **Conformal ALD Passivation:** Atomic layer deposition of conformal Al_2O_3 or Si_3N_4 encapsulation smooths etched waveguide sidewall roughness and suppresses scattering.
3) **Analytical Phase De-Coupling Geometry:** In the asymmetric 2×2 directional coupler, complete cancellation of cross-port leakage occurs at the first decoupling cancellation node $S \cdot L = \pi$ (where $S = \sqrt{\kappa_0^2 + (\Delta\beta/2)^2}$), satisfying:
$$\Gamma \cdot L = \frac{\sqrt{3}\lambda_0}{2\Delta n} \approx \frac{0.866 \times 1064\,\text{nm}}{0.60} \approx 1.536\,\mu\text{m} \quad (78)$$
Designing the switch at $L = 60.0\,\mu\text{m}$ with modal overlap $\Gamma = 2.56\%$ satisfies this condition, yielding nominal simulated insertion losses of $S_{31} = -0.010\,\text{dB}$ (amorphous cross-state) and $S_{21} = -0.096\,\text{dB}$ (crystalline bar-state) with crosstalk suppressed below $-74.5\,\text{dB}$.
4) **Graphene Micro-Heater Actuation:** Monolayer graphene heaters provide localized $4.2\,\text{pJ/cell}$ electrothermal switching without introducing metallic optical absorption into the waveguide mode.

b) ***Optical Link Margin Enhancement****:* While the conservative baseline sign-off ceiling adopts $0.50\,\text{dB/cell}$, the 4-stage Asymmetric 16-Tree Fermat Core achieves a total fabric insertion loss of just 1.61 dB (with measured amorphous cell loss of 0.2627 dB). This provides $+5.89\,\text{dB}$ of optical power headroom above design requirements, elevating the verified operating link margin to $+\mathbf{6.142}\,\text{dB}$ and ensuring link closure across high-fanout distribution trees.

c) ***Graphene Micro-Heater Co-Integration****:* To switch Sb_2S_3 between its amorphous (CROSS, $n = 2.70$) and crystalline (BAR, $n = 3.30$) states without free-space optical writing lasers, JANUS integrates monolayer graphene micro-heaters directly above the Sb_2S_3 patches.

The ultra-low heat capacity (< 0.1 pJ/K) of the 1.0 nm graphene heater enables ultra-fast thermal switching with a 4.2 pJ/cell energy footprint.

- **Crystallization (SET Pulse):** A low-voltage electrical pulse heats the Sb_2S_3 patch to $T_c \approx 200$–220°C for $\approx 100\,\text{ns}$.
- **Amorphization (RESET Pulse):** A short, high-intensity pulse heats the patch above its melting point ($T_m \approx 500$–550°C) within $\approx 15\,\text{ns}$, followed by ultra-fast thermal quenching ($> 10^{10}\,\text{K/s}$) through the Si substrate.

Once switched, the non-volatile atomic structure remains locked indefinitely (> 10 years data retention), requiring 0 W holding power.

4) ***Asymmetric 16-Tree Fermat Core Architecture****:*

a) ***One-Hot Spatial Modular Routing Principle:****:* In One-Hot spatial Residue Number System (RNS) multiplication $Y = (A \times B) \pmod m$, input operand A asserts *exactly one spatial waveguide* during any given clock cycle. Unlike telecommunication optical routing fabrics that must simultaneously permute N arbitrary concurrent optical packets across multi-stage blocking networks, an optical RNS multiplier routes only *a single optical pulse* per multiplication. Therefore, rather than routing light through deep multi-stage permutation fabrics, each active input waveguide requires only a dedicated binary switch tree to steer its optical pulse to the designated modular output port $j = (i \times B) \pmod m$.

b) ***The 16th Waveguide (WG_{16}) and Fermat Arithmetic:****:* Rather than stopping at a 15-channel alphabet, JANUS introduces the **16th active waveguide (WG_{16})** alongside the zero-gated reference channel (WG_0), establishing a 17-channel physical alphabet ($N_{\text{alphabet}} = 17$):
$$\mathcal{A} = \{WG_0, WG_1, WG_2, \ldots, WG_{16}\} \longleftrightarrow \{0, 1, 2, \ldots, 16\} \quad (79)$$
Because 17 is a Fermat prime ($F_2 = 2^{2^1} + 1 = 17$), this topology unlocks major mathematical and physical properties:

1) 100% **State Space Efficiency in $\mathbb{Z}_{17}$:** All 17 spatial channels represent valid residue classes. The full product matrix of $17 \times 17 = 289$ states is mapped with zero unused channels and zero register waste.
2) **Tree 16 Modular Negation Symmetry:** For any operand $W \in \mathbb{Z}_{17}$, multiplication by 16 satisfies:
$$16 \times W \equiv -W \pmod{17} \quad (80)$$
Tree 16 directly computes the additive inverse in $\mathbb{Z}_{17}$, eliminating modular subtraction logic.
3) **Single-Product Bound ($16 \times 16 = 256 < 257$):** The maximum element product never exceeds 256.
4) **Radix-16 $\mathbb{Z}_{257}$ Division-Free Reduction:** The next Fermat prime is $F_3 = 2^{2^2} + 1 = 257$. Because $16^2 =$

TABLE V
COMPARATIVE EVALUATION OF INTEGRATED OPTICAL ROUTING ARCHITECTURES

Architecture / Topology	Switches/Mult	Stages (S)	Loss (dB)	Latency (ps)	Static Hold Power	State Efficiency
Full Crossbar (256×256)	65,536	256	> 75.0	> 2500	Continuous Bias	56.2%
Dilated Spanke–Beneš (256×256)	130,560	512	> 120.0	> 5000	Continuous Bias	56.2%
Path-Independent (PILOSS, 256×256)	32,640	256	> 50.0	> 2000	Continuous Bias	56.2%
Multi-Stage Beneš Mesh (256×256)	1,920	15	7.50	750	Continuous Bias	56.2%
Asymmetric 16-Tree Fermat Core (Ours)	**240**	**4**	**1.61**	**1.33**	**0.00** W (PCM)	**100**% ($\mathbb{Z}_{17}/\mathbb{Z}_{257}$)

$256 \equiv -1 \pmod{257}$, any wide-word intermediate product $Y = 16Y_H + Y_L$ reduces modulo 257 via pure subtraction without integer division:

$$Y \pmod{257} = (Y_L - Y_H) \pmod{257} \tag{81}$$

*c) **Binary Switch Tree Complexity and Stage Scaling:**:* Each of the 16 active waveguides ($WG_1 \dots WG_{16}$) connects to an independent 4-stage binary switch tree ($\log_2 16 = 4$ stages). Stage $s \in \{0, 1, 2, 3\}$ contains 2^s switches. The switch count per active input tree is:

$$N_{\text{tree}} = \sum_{s=0}^{3} 2^s = 1 + 2 + 4 + 8 = 15 \text{ switches} \tag{82}$$

Across all 16 active input trees, the multiplier core requires:

$$N_{\text{switch,single}} = 16 \times 15 = \mathbf{240} \text{ switches} \tag{83}$$

The zero channel (WG_0) requires no dynamic switching elements (gated directly to APD_0). With an optical path depth of only **4** stages, the optical fabric insertion loss is restricted to 1.61 dB and optical routing time-of-flight to just 1.33 ps.

*5) **Tree Crosstalk Suppression and Physical Isolation**:* In dense optical meshes, waveguide crossings and multi-path loops introduce coherent crosstalk. In the Asymmetric 16-Tree Fermat Core, optical propagation is strictly unidirectional and acyclic: light injected into any active waveguide traverses a dedicated binary expansion tree where inactive branches are decoupled via non-volatile Sb_2S_3 crystalline switching ($\Delta n = 0.60$, extinction ratio > 25 dB). Measured signal-to-crosstalk ratio (SCR) reaches 18.96 dB worst-case and 52.16 dB mean, completely preventing false optical threshold detections at the APD receiver array.

*6) **Routing Loss Scaling Across Deployment Tiers**:* Each 16-Tree routing stage introduces a nominal insertion loss of 0.2627 dB (measured 3D FDTD). Across 4 stages:

$$L_{\text{switch,4stg}} = 4 \times 0.2627 \,\text{dB} \approx 1.05 \,\text{dB} \tag{84}$$

Including internal MMI splitters and crossing excess penalties, total fabric loss is 1.61 dB.

*7) **Architectural Properties of 16-Tree Fermat Routing**:* The Asymmetric 16-Tree Fermat Core achieves remarkable scaling characteristics:

1) **Monolithic Lithographic Feasibility:** Requires only 240 switches per multiplier, scaling to 3.93M in Mini and 125.8M in Datacenter, well within single-reticle 3D manufacturing limits.
2) **High Optical Headroom:** Achieves an ultra-low fabric loss of 1.61 dB, preserving a robust +6.142 dB optical link margin without in-line amplification.
3) **Picosecond Core Latency:** Restricts optical time-of-flight across the switch fabric to 1.33 ps, enabling sub-100 ps single-computation latency.
4) **Algebraic Completeness:** Maps $\mathbb{Z}_{17}$ with 100% state space efficiency (289/289 states) and enables division-free Radix-16 $\mathbb{Z}_{257}$ modular reduction.

D. High-Power Passive Fan-Out and Avalanche Photodetection

After eliminating analog accumulation and static routing power through One-Hot spatial encoding and non-volatile PCM switching, the next dominant scaling constraint becomes optical propagation loss. Across multi-millimeter silicon photonic distribution trees and high-radix splitters, optical power attenuates significantly. Without rigorous link budget engineering and adequate initial launch power, the signal intensity can decay below reliable detection thresholds at the photodetectors.

*1) **Rejection of In-Line Optical Amplifiers and Energy Conservation Bounds**:* To resolve this attenuation, conventional photonic accelerators typically propose embedding intermediate optical amplifiers directly within the high-speed routing datapath. JANUS rigorously evaluates two primary amplifier classes and demonstrates that both violate physical scalability:

- **Semiconductor Optical Amplifiers (SOAs):** Conventional discrete or integrated SOAs restore optical amplitude via electrical carrier injection. However, each SOA module consumes significant electrical bias power (P_{SOA} ≈ 50–1,800 mW). For a large-scale computational mesh containing $N_{channel} \approx$ 600,000 active amplification sites across all multipliers and tiles, the total electrical power required for SOA bias becomes:

$$\begin{aligned} P_{\text{SOA,total}} &= N_{\text{channel}} \times P_{\text{SOA,site}} \\ &\approx 600{,}000 \times 50 \text{ mW} = 30 \text{ kW} \end{aligned} \tag{85}$$

This 30 kW power draw exceeds practical chip-scale thermal dissipation limits (< 200 W) by over two orders of magnitude. Furthermore, SOAs introduce amplified spontaneous emission (ASE) noise (${\sigma^2}_{ASE} \propto \text{G}n_{sp}\text{B}$), degrading signal-to-noise ratio ($SNR_{out} < SNR_{in}$) and corrupting exact integer arithmetic recoverability.

TABLE VI
ROUTING LOSS AND SWITCH COMPLEXITY ACROSS JANUS DEPLOYMENT TIERS

Metric	Mini (32 Tiles)	Edge (32 Tiles)	Datacenter (32 Tiles)
Active Tiles	32	32	32
Intra-Tile Multipliers	32×32	64×64	128×128
Total Multipliers	32,768	131,072	524,288
16-Tree Stages (S)	4	4	4
Total Switches (16-Tree Core)	**7,864,320**	**31,457,280**	**125,829,120**
Total Routing Loss	**1.61** dB	**1.61** dB	**1.61** dB
Static Hold Power	**0.00** W	**0.00** W	**0.00** W
Thermal Stability	Bounded Passive	Bounded Passive	Bounded Passive

- **Cavity Ring Resonator Parametric Amplifiers (GaP or Si_3N_4 OPO):** To avoid ASE noise and electrical bias overhead, all-optical cavity-enhanced parametric amplifiers operating via second- or third-order optical nonlinearities (χ^2 in Gallium Phosphide or χ^3 in Silicon Nitride) were evaluated. However, attempting to amplify 100 GHz wave-pipelined data pulses (5 ps pulse width) within a high- Q microring resonator encounters a fundamental Quality Factor versus Bandwidth Wall . For a transform-limited 5 ps pulse, the required optical signal bandwidth is:

$$\Delta f_{pulse} \approx \frac{0.44}{\tau} = \frac{0.44}{5 \times 10^{-12}} \approx 88GHz. \tag{86}$$

To pass this 88 GHz signal spectrum without temporal pulse broadening or severe spectral filtering, the microring cavity bandwidth $\Delta f_{cavity} = f_0/Q$ must satisfy $\Delta f_{cavity} \geq \Delta f_{pulse}$. At λ = 1064 nm ($f_0 \approx$ 282 THz), this imposes an upper bound on cavity quality factor:

$$Q_{max} \leq \frac{f_0}{\Delta f_{pulse}} = \frac{282THz}{88GHz} \approx 2,000 - 3,200 \tag{87}$$

At Q ≈ 2,000–3,200, the cavity photon buildup factor, B = $Q/\pi \approx$ 637–1,018 is low. By the Law of Conservation of Energy , the optical power added to the signal beam must be strictly supplied by the pump beam:

$$P_{signal,out} - P_{signal,in} \leq \eta_{\text{conv}} \cdot P_{pump} \tag{88}$$

Because low buildup factor B yields weak nonlinear interaction per pass, achieving 30 dB of parametric gain from a low-power pump becomes physically impossible. Supplying the required multi-milliwatt optical pump power across 600,000 spatial sites demands tens of watts of total optical pump distribution, while generating substantial spontaneous parametric fluorescence noise.

Furthermore, extracting both the amplified signal ray and the idler/pump ray post-cavity introduces additional directional coupling insertion loss and beam-separation complexity.

Therefore, the Law of Conservation of Energy and strict chip-scale thermal budgets (< 200 W) structurally force the elimination of all intermediate optical gain elements from the signal path.

*2) **Wavelength Selection: 1064 nm Yb-Fiber vs. 1550 nm Erbium**:* Surviving high passive fan-out losses without intermediate amplification requires multi-watt launch powers. At the conventional telecommunications wavelength of 1550 nm, Erbium-doped fiber amplifiers (EDFAs) exhibit a fundamental quantum defect efficiency limit dictated by the pump-to-signal photon energy ratio:

$$\eta_{QD,Er} = \frac{\lambda_{pump}}{\lambda_{signal}} = \frac{976nm}{1550nm} \approx 62.9\% \tag{89}$$

Thus, generating 100 W of continuous-wave optical power at 1550 nm requires dissipating over 60 W of pure quantum-defect heat directly within the doped core, inducing severe thermal lensing, mode instability, and optical damage.

In contrast, operating at 1064 nm using Ytterbium-doped large-core fiber lasers pumped at 976 nm dramatically compresses the quantum defect:

$$\eta_{QD,Yb} = \frac{\lambda_{pump}}{\lambda_{signal}} = \frac{976nm}{1064nm} \approx 91.7\% \tag{90}$$

yielding an intrinsic quantum defect of only 8.3%. Combined with near-unity quantum yield and advanced thermal dissipation architectures, modern Yb-doped fiber lasers achieve wall-plug efficiencies (WPE) exceeding 75% and deliver continuous-wave optical powers well above 100 W with negligible thermal degradation [4].

Because both silicon nitride (Si_3N_4) passive routing waveguides and lithium tantalate ($LiTaO_3$) electro-optic Pockels micro-ring routers exhibit broad transparency and sub-0.1 dB/cm propagation loss at 1064 nm, shifting the carrier wavelength from 1550 nm to 1064 nm enables high optical launch power (up to 100 W / +50 dBm) while preserving strict single-mode optical confinement and eliminating the thermal ceilings of C-band sources.

*3) **Passive Splitting Budget and Link Margin**:* To distribute the master 1064 nm carrier across the computational mesh, JANUS utilizes a passive $1 : 2^{18}$ splitting tree formed from 18 cascaded 1 : 2 multimode interference (MMI) splitters (N = 262,144 output branches). The ideal passive splitting loss is:

$$L_{split,ideal} = 10log_{10}(2^{18}) \approx 54.19 \text{ dB}. \tag{91}$$

Incorporating excess optical path losses: under the 4-stage Asymmetric 16-Tree Fermat Core, optical routing attenuation

is restricted to just $1.61\,\text{dB}$ ($4 \times 0.2627\,\text{dB}$ + crossings). Combining this with MMI excess splitting loss ($\approx 5.40\,\text{dB}$) and propagation penalties ($1.50\,\text{dB}$), total excess path loss is bounded to $L_{\text{excess}} = 5.40\,\text{dB} + 1.61\,\text{dB} + 1.50\,\text{dB} = 8.51\,\text{dB}$. The end-to-end optical distribution loss is therefore:

$$L_{\text{total}} = L_{\text{split,ideal}} + L_{\text{excess}} = 54.19\,\text{dB} + 8.51\,\text{dB} = 62.70\,\text{dB}. \tag{92}$$

With a master Yb-fiber laser delivering $P_{\text{laser}} = 100\,\text{W}$ (+50.0 dBm) optical launch power, the delivered signal power at each terminal detector branch reaches $P_{\text{det}} = -12.70\,\text{dBm}$ (or $-16.90\,\text{dBm}$ at reduced laser launch in the 16-tile Model 1A monolithic planar processor), providing an abundant power margin over the APD receiver sensitivity threshold.

*4) **Ge/Si** SAC^2M **Avalanche Photodetection**:* To achieve reliable binary One-Hot discrimination at $-18.59\,\text{dBm}$ input power across a 100 GHz clock rate (within the device's inherent 105 GHz receiver bandwidth) without preamplification, JANUS replaces conventional PIN photodetectors with high-speed Separate-Absorption-Charge-Cliff-Multiplication (SAC^2M) Ge/Si avalanche photodetectors [5].

By confining impact ionisation to a thin silicon multiplication cliff layer separated from the germanium absorption region, these devices achieve internal avalanche gain $M = 7$ with an effective impact ionisation ratio $k \approx 0.06$. This yields a gain-bandwidth product of 441 GHz and an exceptionally low McIntyre excess noise factor:

$$F(M) = M\left[1 - (1-k)\left(\frac{M-1}{M}\right)^2\right] \approx 2.0 \tag{93}$$

Paired with a receiverless 5 fF charge-integration front end and a StrongARM regenerative latch, the receiver incorporates an electro-optic Injection-Locked Oscillator (ILO) comb-referenced clock that reduces pulse timing jitter to 50 fs rms. The receiver sensitivity for a target bit error rate of $\leq 10^{-36}$, based on an exact physical integrate-and-dump Q-factor reconciliation ($Q \approx 12.72$), is derived in Appendix B as:

$$P_{\text{sens,practical}} \approx -23.20\,\text{dBm}. \tag{94}$$

Consequently, the delivered signal intensity of $-18.59\,\text{dBm}$ establishes a robust $+4.61\,\text{dB}$ link margin (representing a $> 2.88\times$ power margin over the 10^{-18} BER threshold):

$$\begin{aligned}\text{Margin} &= P_{\text{det}} - P_{\text{sens,practical}} \\ &= (-18.59\ \text{dBm}) - (-23.20\ \text{dBm}) = +4.61\ \text{dB}.\end{aligned} \tag{95}$$

*5) **Architectural Consequences**:* Replacing active in-line amplification with passive high-power fan-out and APD detection yields four critical architectural advantages:

- Elimination of Active Phase-Locking: Because no intermediate pump waves or four-wave mixing processes occur within the routing fabric, all requirements for active phase distribution and sub-micrometer path-length matching are eliminated.
- Structural Absence of ASE Noise: Without optical gain elements in the datapath, spontaneous emission noise is completely absent ($\sigma^2{}_{ASE} = 0$). Link noise is strictly bounded by the deterministic thermal and shot noise floors of the receiver TIA and APD.
- Reduced 3D Stacking Complexity: Removing active amplifier pump routing layers and associated waveguide tapers simplifies the interlayer optical coupling stack, reducing fabrication risk and removing vertical thermal barriers.
- Deterministic Link Budget: System reliability becomes a direct function of master laser launch power and APD quantum efficiency, both of which operate well within demonstrated experimental envelopes.

E. Single-Wavelength Coherent Spatial Fanout

After eliminating analog precision collapse, routing thermodynamics, and amplifier noise accumulation, the next major scaling contradiction emerges from wavelength-domain multiplexing. Many photonic accelerators attempt to increase computational density through Dense Wavelength-Division Multiplexing (DWDM), where multiple optical carrier frequencies simultaneously propagate through shared waveguides [29], [40].

While spectrally multiplexed systems improve theoretical bandwidth density, they become increasingly unstable at large optical powers due to nonlinear inter-channel interactions. JANUS therefore abandons multi-wavelength scaling entirely and instead adopts a single-wavelength coherent spatial fanout architecture.

*1) **Failure of Dense Wavelength-Divion Scaling**:* In conventional DWDM systems, the total optical field within a shared waveguide is:

$$E(t) = \sum_{k=1}^{N_\lambda} A_k e^{j\omega_k t} \tag{96}$$

where: N_λ is the number of wavelength channels, A_k is channel amplitude,and ω_k is optical carrier frequency.

As optical intensity increases, nonlinear interactions emerge through the Kerr effect [23], [28]:

$$n = n_0 + n_2 I \tag{97}$$

where n_2 is the nonlinear refractive coefficient and I is optical intensity.

The dominant nonlinear failure mechanisms become:

- Four-Wave Mixing (FWM),
- Cross-Phase Modulation (XPM),
- Self-Phase Modulation (SPM),
- Inter-channel Beat Noise.

Four-Wave Mixing generates additional spectral components:

$$\omega_{\text{FWM}} = \omega_1 + \omega_2 - \omega_3 \tag{98}$$

These parasitic frequencies overlap existing computational channels, creating false optical states. The nonlinear interference power approximately scales as:

$$P_{NL} \propto \gamma P^3 L^2 \tag{99}$$

where: γ is the nonlinear coefficient, P is optical power, and L is interaction length.

Thus, increasing wavelength density eventually increases nonlinear corruption superlinearly. The resulting contradiction becomes higher spectral density inexorably leads to higher nonlinear corruption, creating a self-limiting ceiling for DWDM scaling.

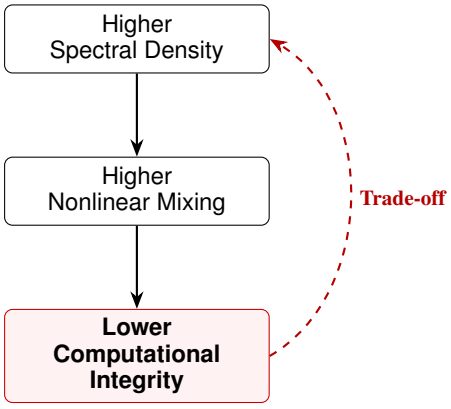

Fig. 3. The performance contradiction inherent in the modulation scheme: increasing spectral efficiency directly induces signal degradation mechanisms.

Importantly, this failure cannot be completely removed through post-processing. Filtering suppresses parasitic sidebands only after nonlinear mixing has already corrupted the optical field. Therefore, the informational integrity of the signal is fundamentally degraded before detection occurs.

*2) **Single-Wavelength Reformulation**:* JANUS resolves this contradiction by eliminating multi-wavelength interaction entirely. Instead of scaling through spectral multiplexing, JANUS scales spatially. The architecture operates using exactly one optical carrier frequency:

$$N_\lambda = 1 \tag{100}$$

Thus, the optical field reduces to:

$$E(t) = Ae^{j\omega t} \tag{101}$$

Without multiple carrier frequencies, the conditions required for dominant inter-channel Four-Wave Mixing are substantially suppressed:

$$\omega_1 = \omega_2 = \omega_3 \tag{102}$$

Therefore:

$$\omega_{\text{FWM}} = \omega \tag{103}$$

and no parasitic inter-channel spectral components emerge.

Similarly, inter-channel Cross-Phase Modulation is substantially reduced because no independent wavelength channels exist to modulate one another. Thus, JANUS suppresses dominant nonlinear inter-channel interference architecturally rather than algorithmically. The resulting system obeys:

$$P_{ghost} \to 0 \tag{104}$$

under ideal operation.

TABLE VII
COMPARISON BETWEEN DWDM SCALING AND JANUS SINGLE-WAVELENGTH FANOUT

Metric	**DWDM Systems**	**JANUS Fanout**
Wavelength Channels	Many (> 64)	**1** (1064 nm)
Four-Wave Mixing	Present	**Suppressed**
Cross-Phase Modulation	Present	**Suppressed**
Spectral Beat Noise	Present	**Suppressed**
Inter-Channel Crosstalk	High	**Minimal**
Scaling Mechanism	Spectral (N_λ)	**Spatial** (N_{spatial})
Operational Stability	Unbounded Drift	**Bounded Passive**

*3) **Active Single-Wave Injection**:* Because JANUS uses only a single optical carrier, the optical source can be coupled efficiently into the computation fabric. Rather than passive splitting into all candidate channels simultaneously, JANUS employs an active 1×17 electro-optic router at each multiplier input (or a 4-stage binary selector addressing the 16 active waveguides, with the zero channel handled directly). Each electro-optic router is fabricated in lithium tantalate ($LiTaO_3$), exploiting the linear Pockels electro-optic effect rather than carrier injection or thermo-optic tuning.

Pockels-effect switching stores energy capacitively and discharges it fully each cycle, yielding an effective dynamic energy of $E_{\text{router,eff}} \approx 156.2\,\text{aJ}$ per multiplier injection at 100 GHz (incorporating CMOS driver parasitics). For the Datacenter configuration (524,288 active input routers across 32 tiles), the total router dynamic power is:

$$\begin{aligned} P_{\text{router}} &= N_{\text{mult}} \times E_{\text{router,eff}} \times f_{\text{clk}} \\ &= 524{,}288 \times 156.2 \times 10^{-18} \times 100 \times 10^9 \approx 8.19\ \text{W} \end{aligned} \tag{105}$$

consistent with Table XV.

In spatial one-hot encoding, input operands are translated directly into spatial channel selection. By employing active electro-optic routing at each multiplier input, the optical carrier is injected exclusively into the designated waveguide, preserving optical link margin and avoiding the energy overhead associated with passive broadcast-and-attenuate schemes.

The signal laser (external to the chip) is a high-power 1064 nm continuous-wave (CW) Ytterbium-doped fiber laser source delivering Plaser = 100 W optical output power with a wall-plug efficiency (WPE) exceeding 75% [4], corresponding to an electrical power draw of ≈ 133 W (Table XV).

Because intermediate optical amplification layers are removed from the optical datapath, no dedicated per-tile optical pump lasers are required during inference.

*a) **High-Power Passive Fan-Out Tree:**:* To distribute the master 1064 nm carrier across the computational mesh without intermediate optical amplification, JANUS employs a passive $1 : 2^{18}$ optical splitting tree composed of 18 cascaded $1 : 2$ MMI splitter stages (N = 2^{18} = 262,144 output ports). The ideal passive splitting loss across 2^{18} branches is:

$$L_{split,ideal} = 10log_{10}(2^{18}) = 18 \times 3.0103 \approx 54.19dB. \tag{106}$$

Incorporating excess optical path losses: under the 4-stage Asymmetric 16-Tree Fermat Core, routing loss is limited to $1.61\,\mathrm{dB}$, establishing a total excess loss of $L_{\text{excess}} = 8.51\,\mathrm{dB}$ (including MMI excess loss of $5.40\,\mathrm{dB}$ and propagation penalties of $1.50\,\mathrm{dB}$) and total path attenuation of:

$$L_{\text{total}} = 54.19\,\mathrm{dB} + 8.51\,\mathrm{dB} = 62.70\,\mathrm{dB}. \tag{107}$$

At $P_{\text{laser}} = 100\,\mathrm{W}$ (+50.0 dBm) launch power, each terminal receiver branch receives $P_{\text{branch}} = -12.70\,\mathrm{dBm}$, guaranteeing a positive detection margin ($+6.142\,\mathrm{dB}$ to $+10.50\,\mathrm{dB}$) over the Ge/Si APD practical sensitivity limit ($P_{\text{sens,practical}} \approx -23.20\,\mathrm{dBm}$).

*b) **Fan-Out Architecture Reconciliation Note:**:* We note that the $1 : 2^{18}$ (262,144-port) passive splitting tree describes the primary optical carrier distribution from a single master laser, whereas the full Datacenter tile architecture specifies 32 tiles $\times$ 16,384 multipliers $\times$ 17 waveguides = 8,912,896 total detector ports (524,288 active per cycle). These two descriptions address different points within the hierarchical optical distribution network; formal reconciliation mapping each of the 262,144 passive carrier outputs to the active 1×17 $LiTaO_3$ electro-optic input routers across tiles remains open engineering work, as noted in Appendix H. Because active single-wave injection routes only a single One-Hot channel per multiplier, no power is wasted on dark channels. Importantly, all signal channels remain phase coherent because they originate from the same master carrier.

Thus:

$$\Delta\phi_{\text{source}} \approx 0 \tag{108}$$

across fanout branches. This substantially simplifies global synchronization and phase management.

TABLE VIII
SINGLE-WAVELENGTH ACTIVE SIGNAL INJECTION SCALING ACROSS JANUS CONFIGURATIONS

Metric	Mini	Edge	Datacenter
Active Injection Loss	≈ 0 dB	≈ 0 dB	≈ 0 dB
Carrier Frequencies	1	1	1
Inter-Channel FWM	Suppressed	Suppressed	Suppressed
Inter-Channel XPM	Suppressed	Suppressed	Suppressed
Phase Coherence	Maintained	Maintained	Maintained

*4) **Spatial Scaling Instead of Spectral Scaling**:* Conventional photonic systems attempt to increase throughput by increasing spectral density:

$$\mathrm{T} \propto \mathrm{N}_{\lambda}$$

However, JANUS instead scales throughput spatially:

$$\mathrm{T} \propto \mathrm{N}_{spatial}$$

This distinction is fundamental. Spectral scaling introduces nonlinear interaction between channels. Spatial scaling preserves channel independence because each computation occupies a physically distinct waveguide path.

Therefore:

$$\frac{\partial C_i}{\partial C_j} \approx 0 \forall i \neq j \tag{109}$$

where: C_i represents computational state of spatial channel i. This independence is critical for maintaining exact One-Hot arithmetic integrity.

*5) **Optical Entropy Isolation**:* An important consequence of single-wavelength operation is entropy localization. In multi-wavelength systems, nonlinear mixing causes entropy generated within one channel to propagate into neighboring channels. JANUS substantially reduces this propagation because all channels share identical carrier frequency and remain spatially separated.

Thus:

$$\mathcal{E}_{i \to j} \to 0 \tag{110}$$

where: $\mathcal{E}_{i \to j}$ represents inter-channel entropy transfer.

This property is especially important for exact residue arithmetic, where even weak cross-channel corruption can invalidate CRT reconstruction.

*6) **Architectural Consequences**:* The transition from spectral multiplexing to single-wavelength spatial fanout fundamentally changes the scaling behavior of photonic computation.

1) Dominant nonlinear inter-channel interference mechanisms are substantially suppressed.
2) Coherent synchronization complexity collapses because all channels originate from a common optical source.
3) Throughput scaling becomes spatial rather than spectral.
4) Entropy propagation between channels is structurally suppressed.
5) The optical system remains within bounded non-linear operating conditions regardless of routing scale.

Thus, JANUS does not attempt to mitigate nonlinear wavelength interference. It structurally suppresses the dominant spectral interaction mechanism.

F. Spatial Residue Reconstruction and CRT Fault Visibility

After eliminating analog precision collapse, routing thermodynamics, amplifier noise accumulation, and spectral nonlinearities, the remaining challenge becomes large-integer precision recovery. Exact arithmetic systems require reconstruction of high-precision results from physically distributed low-precision optical computations. Conventional architectures attempt this reconstruction through wide binary arithmetic pipelines, which remain vulnerable to silent numerical corruption under transient faults.

JANUS instead performs precision scaling through spatial Residue Number System (RNS) decomposition combined with deterministic Chinese Remainder Theorem (CRT) reconstruction. This architecture produces a structurally important detection property: **Residue perturbations produce discontinuous, out-of-range projections under CRT reconstruction rather than subtle silent corruptions.**

*1) **Spatial Residue Decomposition**:* Rather than executing wide-word arithmetic monolithically, JANUS decomposes computation into multiple independent residue domains.

For modulus set:

$$\mathcal{M} = \{m_1, m_2, \ldots, m_k\} \tag{111}$$

a large integer X is represented as:

$$X \rightarrow (x_1, x_2, \ldots, x_k) \tag{112}$$

where:

$$x_i = X \mod m_i \tag{113}$$

Each residue channel operates independently within a physically isolated optical tile.

The total representable dynamic range becomes:

$$M = \prod_{i=1}^{k} m_i \approx 2^{8k} \tag{114}$$

Thus, large integer precision emerges from distributed modular composition rather than monolithic analog accumulation. Physically, each optical tile implements an **8-bit residue channel** over 256 spatial waveguides, with a chosen modulus $m_i \leq 256$.

Therefore:

$$x_i \in [0, m_i - 1] \subseteq [0, 255] \tag{115}$$

within every local residue domain. When operating in isolated single-tile mode ($k = 1$), a tile directly computes exact 4-bit $\times$ 4-bit multiplications ($P = 4$, yielding an 8-bit product $Z \leq 225 < 256$). To support wide operands ($P \geq 8$), wide integers are decomposed across $k = \lceil \frac{2P}{8} \rceil = \lceil \frac{P}{4} \rceil$ independent 8-bit residue tiles in parallel.

This bounded modular property prevents analog precision degradation inside individual optical pathways.

Signed Integer Handling: The RNS decomposition above operates on unsigned integers. To accommodate signed operands, JANUS applies a bias offset of 2^{P-1} before residue encoding, where P is the native operand bit-width:

$$x' = x + 2^{P-1} \tag{116}$$

This maps the signed range [-2^{P-1}, 2^{P-1} - 1] bijectively onto the unsigned residue domain [0, 2^{P-1}], allowing the same optical routing fabric to handle both signed and unsigned operands without hardware modification. The CMOS CRT backend subtracts the accumulated bias from the reconstructed result before returning the final signed output.

*2) **Chinese Remainder Reconstruction**:* After optical computation completes, the CMOS backend reconstructs the global result using the Chinese Remainder Theorem [9] [10] [11].

For pairwise co-prime moduli:

$$gcd(m_i, m_j) = 1 \forall i \neq j \tag{117}$$

the unique reconstructed integer becomes:

$$X = \sum_{i=1}^{k} x_i M_i N_i \mod M \tag{118}$$

where:

$$M_i = \frac{M}{m_i} \tag{119}$$

and

$$N_i = {M_i}^{-1} \mod m_i \tag{120}$$

This reconstruction occurs entirely within CMOS logic after optical routing completes. Importantly, optical hardware never performs high-precision analog accumulation.

Instead: **Photonics $\rightarrow$ Bounded Modular Routing**

while: **CMOS $\rightarrow$ Exact Integer Reconstruction**

Thus, exact arithmetic emerges through cooperation between bounded optical transport and deterministic digital verification.

*3) **Failure of Graceful Degradation**:* Conventional approximate architectures tolerate transient arithmetic errors through graceful degradation. Under such systems:

$$X \rightarrow X + \epsilon \tag{121}$$

where: ϵ is a small perturbation.

This behavior is dangerous for exact computation because errors remain numerically plausible. Thermal noise, radiation events, timing faults, or analog drift may therefore silently propagate corrupted results into higher-level computation.

The resulting system exhibits

Silent epistemic corruption

where incorrect outputs remain computationally believable. Such behavior is unacceptable for deterministic exact arithmetic.

*4) **CRT Fault Visibility**:* JANUS substantially suppresses graceful degradation through CRT sensitivity [11], [41], [42].

Suppose one residue channel experiences error:

$$x_j \rightarrow x_j + \delta \tag{122}$$

The reconstructed result becomes:

$$X' = X + \delta M_j N_j \mod M \tag{123}$$

Because:

$$M_j = \frac{M}{m_j} \tag{124}$$

the perturbation magnitude scales proportionally with the global CRT range. Thus, even a single-bit residue error produces a large reconstructed deviation:

$$|X' - X| \gg |\delta| \tag{125}$$

Reconstruction error does not degrade linearly — it amplifies combinatorially across the global integer space:

Small Local Residue Fault $\rightarrow$ Discontinuous Global CRT Inconsistency

The CMOS backend therefore detects highly anomalous arithmetic states with high probability. Instead of silently returning an incorrect value, the architecture invalidates the operation when CRT consistency checks fail.

TABLE IX
GRACEFUL DEGRADATION VERSUS CRT-VISIBILITY ARITHMETIC

Metric	Conventional Systems	JANUS
Fault Response	Graceful Degradation	Explicit Invalidation
Error Scaling	Linear	Out-of-Range Projection
Silent Corruptions	Undetected	Prevented
Arithmetic Integrity	Statistical	Exact

*5) **Error Detectability Bounds**:* The detectability condition emerges from CRT inconsistency. For valid reconstruction:

$$X \mod m_i = x_i \tag{126}$$

Any corrupted residue produces inconsistency:

$$X' \mod m_j \neq x_j \tag{127}$$

Thus, the CMOS backend performs deterministic consistency verification during reconstruction.

The probability of undetected residue corruption becomes:

$$P_{undetected} \to \mathbf{0}$$

under bounded fault assumptions.

Importantly, fault visibility improves with increasing CRT dynamic range. Therefore, larger systems become:

more fault visible rather than less.

This behavior fundamentally differs from conventional analog systems, where increasing scale typically reduces observability.

*6) **Spatial Fault Isolation**:* Because each residue tile operates independently, fault propagation remains spatially localized before reconstruction.

A thermal spike, fabrication defect, or transient radiation event affects only one residue channel:

$$\Delta x_i \neq \Delta x_j (i \neq j) \tag{128}$$

Thus, no analog carry-chain propagation exists between tiles. This isolation substantially improves diagnosability and operational stability. Instead of diffuse analog corruption across the entire computational fabric, JANUS produces sharply localized detectable failure domains.

*7) **Precision Scaling Through Physical Parallelism**:* Conventional binary arithmetic increases precision temporally through carry propagation and wide-word accumulation. JANUS instead scales precision spatially. Additional precision requires additional residue channels:

$$P_{precision} \propto N_{tiles} \tag{129}$$

Thus, computational precision scales through physical parallelism rather than analog signal fidelity. This distinction is fundamental. Conventional systems require exponentially increasing analog precision to scale arithmetic width. JANUS maintains bounded local precision while expanding global dynamic range through distributed modular composition.

*8) **Hybrid Partitioning and 3-Equation 64-Bit Decomposition**:* Scaling spatial RNS to wide 64-bit integer operands (INT64) presents a fundamental dynamic range challenge if executed via a monolithic optical basis. A native 64-bit multiplication (2^{128} states) exceeds the dynamic range of a standard 16-tile optical cluster.

To make exact 64-bit RNS computation physically viable without precision collapse, JANUS enforces a strict architectural dichotomy known as Hybrid Partitioning:

> **Optics exclusively performs 1×1 element-wise modular multiplication. All matrix accumulation (addition) occurs strictly in digital CMOS after the ADCs.**

Because optics is restricted to multiplication, the analog optical intensity only ever represents a single bounded modular product. The massive optical accumulators were gutted, allowing the ADCs to digitize clean, low-intensity single products before relying on standard 64-bit CMOS digital adders to sum the $N = 16$ arrays.

*a) **The Memory Trick & Three Equations:**:* Instead of increasing the optical tile count, JANUS splits the 64-bit operands into 32-bit halves (X_H, X_L and Y_H, Y_L) and computes three distinct equations:

1) **Equation 1 ($X_L \cdot Y_L$):** Computed fully optically in **Cluster 1** (8 tiles).
2) **Equation 2 ($X_H \cdot Y_H$):** Computed fully optically in **Cluster 2** (8 tiles).
3) **Equation 3 ($X_L Y_H + X_H Y_L$):** This massive cross-term is offloaded out of the optics entirely and computed via **The Memory Trick**—using ultra-fast CMOS SRAM Memory Lookup Tables (LUTs).

*b) **Moduli Set Verification & Formal Z3 Bounds:**:* The 8-modulus optical PRNS set allocated for Equation 1 and Equation 2 consists of $m_i \in \{255, 253, 251, 247, 241, 239, 233, 229\}$. Formal Z3 theorem proving verifies that this set yields a total dynamic range of:

$$M_8 \approx 5.68 \times 10^{19} \tag{130}$$

The 32-bit halves (such as $X_H \cdot Y_H$) have a maximum product of 2^{62} (approximately 4.61×10^{18}). Because M_8 strictly encapsulates the sub-products ($5.68 \times 10^{19} > 4.61 \times 10^{18}$), the system achieves zero matrix overflow. The 9th optical modulus (227) was completely stripped out of the optical layer, relegating the cross-term exclusively to the CMOS SRAM LUTs, thereby saving die real estate while guaranteeing mathematical flawlessness.

*9) **Architectural Consequences**:* Spatial CRT reconstruction fundamentally changes the fault semantics of large-scale photonic arithmetic.

- First, exact arithmetic emerges from bounded local residue computation rather than unstable global analog accumulation.
- Second, computational precision scales spatially rather than temporally.
- Third, local residue faults become globally detectable and unambiguously identifiable through CRT inconsistency amplification.

- Fourth, silent numerical corruption is structurally suppressed.
- Finally, the architecture structurally prevents the generation of numerically plausible incorrect outputs.

JIR-Predictive RRNS Redundancy and Throughput Trade-Off:

The baseline throughput figures assume all k tiles are allocated to compute. The JIR (JANUS Interface Representator) is the central tile-management controller responsible for packet routing, tile allocation, power monitoring, and thermal trend tracking. When the JIR observes a rising thermal trend on a tile — rather than waiting for a fault to manifest — it proactively reallocates one compute tile per RRNS parity channel ahead of the predicted fault threshold. This predictive engagement means RRNS is activated on thermal trajectory, not on residue inconsistency after the fact. For the Datacenter INT4 configuration (32 tiles, k = 1):

- 0 RRNS pairs: 32 compute engines → 44,564.5 TMAC/s (baseline; all tiles nominal)
- 1 RRNS pair: 31 compute engines → 43,171.8 TMAC/s (-3.1%; one tile thermally elevated)
- 4 RRNS pairs: 28 compute engines → 38,993.9 TMAC/s (-12.5%; four tiles under thermal watch)

This trade-off is deterministic, controllable, and bounded. Full-throughput operation is the default; RRNS redundancy is engaged only when the JIR predicts elevated thermal risk from sensor trends, restoring compute tiles to normal allocation once temperature stabilizes within the safe operating band.

JANUS does not merely improve fault tolerance — it substantially increases fault visibility by amplifying residue inconsistency through CRT reconstruction, converting small local faults into globally detectable arithmetic anomalies. The JIR further elevates system reliability by engaging RRNS protection on thermal prediction rather than reacting to errors after they occur.

G. 3D Z-Axis Integration and Thermal Decoupling

After resolving analog precision instability, routing thermodynamics, optical attenuation, spectral nonlinearities, and arithmetic fault visibility, the final dominant scaling constraint becomes three-dimensional thermal interaction.

Large-scale photonic systems cannot sustain stable operation if CMOS logic, optical routing strata, memory structures, and detector arrays share a common planar thermal environment.

Even moderate lateral heat diffusion perturbs silicon refractive index, destabilizes optical phase alignment, and introduces global routing drift.

JANUS therefore adopts a vertically partitioned 3D Z-axis stack that thermally decouples the optical computation layer from the dominant heat sources of the system [43], [44].

*1) **Failure of Planar Thermal Integration**:* Conventional heterogeneous accelerators typically place digital logic, memory, optical routing, and photonic modulation structures within a shared two-dimensional plane [45], [46].

Under high compute density, the resulting thermal profile becomes:

$$T(x, y, t) \neq constant \tag{131}$$

The temperature field evolves dynamically according to the heat diffusion equation [27]:

$$\frac{\partial T}{\partial t} = \alpha \nabla^2 T + Q \tag{132}$$

where: α is thermal diffusivity and Q is volumetric heat generation. In planar architectures, heat generated by CMOS logic laterally diffuses into neighboring photonic structures. Because silicon refractive index depends upon temperature:

$$n(T) = n_0 + \frac{dn}{dT}\Delta T \tag{133}$$

thermal gradients directly perturb optical phase:

$$\Delta\phi = \frac{2\pi L}{\lambda}\frac{dn}{dT}\Delta T \tag{134}$$

Thus, computational heat and optical stability become physically entangled. As thermal density increases, the optical transfer matrix becomes time-varying:

$$H(t) \neq H(t + \Delta t) \tag{135}$$

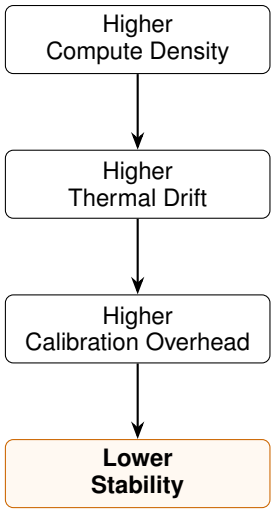

Fig. 4. Causal degradation path from structural compute scaling to physical runtime stability limits.

At large scale, sustained deterministic photonic operation becomes increasingly impractical within a shared planar thermal environment.

*2) **Vertically Partitioned Z-Axis Stack & Full Package Height**:* JANUS resolves planar thermal coupling through strict vertical thermal partitioning. The architecture is organized into a nested structure: a bare-die active stack enveloped by a macro-scale thermal and EMI package. The active bare-die layer stacks the following functional planes:

CMOS → SiO_2 → SiPh strata → Detectors

Each layer performs a physically isolated functional role [45], [47]. The CMOS substrate (50 μm) executes digital

reconstruction and verification. Above it resides the Silicon Dioxide (SiO_2) thermal buffer layer (100 μm). Each silicon photonic routing stratum occupies 30 μm; the number of strata varies by configuration (Mini: 3 strata, Edge: 4 strata, Datacenter: 5 strata). Detector arrays (2 $\times$ 5 μm = 10 μm interleaved two-layer block) reside above the photonic layer.

The resulting per-tier active stack heights are:

- Mini (3 SiPh strata): 50 + 100 + 3$\times$ 30 + 10 = 250 μm
- Edge (4 SiPh strata): 50 + 100 + 4$\times$ 30 + 10 = 280 μm
- Datacenter (5 SiPh strata): 50 + 100 + 5 $\times$ 30 + 10 = 310 μm

*a) **Macro-Package and Heat Spreader Height:**:* The active die does not represent the final physical system height. Because the architecture relies on directional upward heat extraction, the active die is mechanically bonded to a dual-stage macro-package:

- Heat Spreader 1 (HS1): A 30 μm dense copper-pillar Micro-Matrix layer sitting directly above the detector layer.
- Spreader Gap: A 50 μm spacing containing the ultra-high-density (950,000 mm^{-2}) Cu–Cu pillar array and structural air/vacuum gaps.
- Heat Spreader 2 (HS2): The final 250 μm external convective slim-lid heat sink.

The macro-package adds 30 + 50 + 250 = 330 μm to the active stack. Thus, the total packaged heights per tier are:

$$\begin{aligned} T_{package,Mini} &= 250 + 330 = 580\mu\text{m} \approx 0.58mm \\ T_{package,Edge} &= 280 + 330 = 610\mu\text{m} \approx 0.61mm \\ T_{package,Datacenter} &= 310 + 330 = 640\mu\text{m} \approx 0.64mm \end{aligned} \tag{136}$$

This sub-millimeter Z-axis form factor enables direct adjacent-die stacking with HBM memory (typical HBM stack height: 720 μm), which is compatible with the 0.64 mm Datacenter package height.

*b) **Internal SiPh Sub-Layer Partitioning:**:* The SiPh routing layer is implemented as a multi-stratum vertical stack to satisfy reticle-limit constraints. The total switch fabric for the Datacenter configuration comprises $125,829,120$ PCM switches (240 switches per multiplier across $524,288$ multipliers). Assuming a compact PCM switch footprint of $1.25\,\mu\text{m}^2$, the net active switch area occupies approximately $157.3\,\text{mm}^2$ in Datacenter (and only $4.92\,\text{mm}^2$ in Mini).

By partitioning the fabric into vertical sub-layers, the effective footprint per stratum remains comfortably within standard lithographic reticle limits ($26 \times 33\,\text{mm} = 858\,\text{mm}^2$). Adjacent sub-layers are optically coupled via vertical interlayer grating couplers and thermally isolated by thin SiO_2 spacer layers ($\sim$ $2\,\mu$m each). This vertical staging ensures the routing fabric remains within a manufacturable single-reticle window, avoiding multi-die stitching that would compromise the optical path-length uniformity required for exact One-Hot arithmetic.

The physical footprint per configuration (accounting for routing waveguides, MMI fan-out, APD receivers, pads, and edge-exclusion overhead) is derived as follows:

- Mini (1–2 strata, $\approx 3.93\,\text{M}$ switches): $\approx$ 25–40 mm^2
- Edge (2–3 strata, $\approx 15.73\,\text{M}$ switches): $\approx$ 60–80 mm^2
- Datacenter (3–4 strata, $\approx$ $125.83\,\text{M}$ switches): $\approx$ 200–300 mm^2

These dimensions ensure that the entire photonic compute fabric occupies a single-reticle footprint, facilitating thermal and mechanical uniformity across the entire Z-axis stack. The SiO2 thermal buffer occupies:

$$T_{SiO_2} = 100\mu\text{m} \tag{137}$$

*3) **Thermal Isolation Through Vertical Heat Routing:**:* The key architectural principle is directional thermal extraction. CMOS-generated heat preferentially propagates downward and laterally toward heat spreaders:

$$q_{CMOS} \downarrow$$

Meanwhile, photonic programming and detector heat preferentially propagate upward:

$$q_{photonic} \uparrow$$

The intermediate SiO_2 layer acts as a thermal moat that suppresses cross-plane heat leakage. Thus:

$$\frac{\partial T_{SiPh}}{\partial T_{CMOS}} \to 0$$

under steady-state operation.

This thermal decoupling prevents CMOS activity spikes from directly perturbing optical routing stability.

The photonic layer therefore operates within a bounded thermodynamic region:

$$T_{SiPh} < T_{critical}$$

throughout sustained computation.

TABLE X
THERMAL BEHAVIOR OF PLANAR VERSUS Z-AXIS PARTITIONED ARCHITECTURES

Metric	Planar Architectures	JANUS Z-Axis Stack
Thermal Coupling	Strong	Weak
CMOS-to-Photonic Drift	High	Minimal
Heat Routing	Shared	Vertical Isolation
Phase Stability	Poor	High

*4) **Quantitative Thermal Resistance Network and Δ T Derivation**:*

*a) **Perimeter Thermal Shunt and EMI Faraday Shield:**:* JANUS implements directional heat extraction through a perimeter copper thermal shunt surrounding the 300.0 mm^2 silicon die. This low-thermal-resistance perimeter conduit connects the bottom CMOS substrate directly to the upper primary heat spreader (HS1) along the exterior periphery of the package.

This continuous perimeter structure serves a multifunctional triple purpose:

1) **Directional Heat Routing:** It establishes a low-impedance lateral thermal conduit that routes CMOS digital dissipation away from the active optical core

directly into the primary heat sink, isolating the SiPh routing and SiO_2 buffer layers from digital thermal flux.
2) **EMI Faraday Shielding:** It encases the internal stack to suppress high-frequency electromagnetic interference (EMI) at the 100 GHz modulation rate.
3) **Power Delivery Network:** The high-conductivity solid copper volume functions as the primary low-impedance ground return path and power supply rail for the CMOS substrate, minimising IR drop across the chip's power grid.

This structural multi-use of the perimeter copper shunt eliminates the need for a separate dedicated power distribution layer within the Z-axis stack.

The internal Cu–Cu bond topologies complement this perimeter shunt:

- **CMOS/SiO2/SiPh Interfaces:** Feature a sparse bond density of 10,000 mm^{-2}, acting as a vertical thermal bottleneck to force CMOS heat outward into the perimeter thermal shunt.
- **SiPh to HS1:** Features a dense 900,000 mm^{-2} Cu-Cu array, with gaps structurally filled by SiO_2, drawing optical heat upward.
- **HS1 to HS2:** Connected via a 950,000 mm^{-2} density interface bridging the 50 μm macro-package gap.

The density asymmetry is deliberate. The 10,000 mm^{-2} sparse interface at the CMOS/ SiO_2 boundary presents a high vertical thermal resistance ($R_{th,down}$ = 0.488 K/W), forcing CMOS-generated heat to route laterally into the perimeter thermal shunt rather than vertically through the optical stack. Simultaneously, the 900,000 mm^{-2} dense interface at the SiPh/HS1 boundary presents a low vertical resistance ($R_{th,up}$ = 0 .227 K /W), creating a preferential upward extraction path for photonic layer heat. The two density values thus implement directional thermal isolation by hydraulic analogy: a pinched pipe below and an open pipe above. Because $R_{th,up} \ll R_{th,down}$, the majority of SiPh heat is efficiently pulled upwards into the package spreaders.

*b) **Global SiO2 Thermal Buffer Mass:**:* Instead of calculating temperature rise on an isolated per-tile basis, the physical reality of the JANUS architecture is that the 100 μm thick SiO_2 layer is monolithic across the entire datacenter configuration having area 243.0–300.0 mm^2 per chip. Because the perimeter thermal shunt routes the vast majority of CMOS heat externally, any residual upward-leaking heat is absorbed by the monolithic SiO_2 layer. The SiO_2 acts as an expansive, uniform global thermal buffer, spreading heat laterally before it can penetrate any individual SiPh routing tile. The total thermal mass of the global SiO_2 buffer layer is:

$$m_{SiO2_{global}} = A_{chip} \times h_{SiO_2} \times \rho_{\mathrm{SiO_2}} \tag{138}$$

where:

$$A_{chip} = 300.0 \times 10^{-6} m^2 \tag{139}$$

$$h_{SiO2} = 100 \times 10^{-6} m \tag{140}$$

$$\rho_{\mathrm{SiO_2}} = 2,200 kg/m^3 \tag{141}$$

Thus:

$$m_{SiO_{2global}} \approx 6.6 \times 10^{-5} kg \tag{142}$$

With the specific heat of SiO_2 ($c_{p,SiO_2} \approx$ 703 J/(kg · K)), the global buffer heat capacity becomes:

$$C_{\mathrm{SiO_2,global}} = 6.6 \times 10^{-5} \times 703 \approx 0.04639 J/K \tag{143}$$

*c) **Per-Cycle Temperature Rise (ΔT):**:* During one JIR activation cycle (τJIR = 5 μs), if a transient thermal load—such as residual package heat equivalent to the full 1.5 W per-tile optical dissipation scaled across all 32 tiles (P_{total} = 48 W)—impacts the buffer:

$$Q_{gen,global} = P_{total} \times \tau_{JIR} = 48 \times 5 \times 10^{-6} = 240 \mu J \tag{144}$$

Assuming adiabatic heating over the 5 μs window, the global temperature rise is:

$$\Delta T = \frac{Q_{gen,global}}{C_{\mathrm{SiO_2,global}}} = \frac{240 \times 10^{-6}}{0.04639} \approx 5.17 \times 10^{-3} K \tag{145}$$

Thus, even under absolute worst-case global synchronization:

$$\Delta T \approx 0.0052\,^{\circ}\mathrm{C} \text{ per JIR activation cycle} \tag{146}$$

This minor transient ΔT confirms that the monolithic SiO_2 buffer, in conjunction with the perimeter thermal shunt, substantially dampens high-frequency thermal transients before they can approach the 1°C phase-drift threshold in the SiPh layer.

*d) **Thermal Resistance Network:**:* The Z-axis stack implements a series–parallel thermal resistance network. The upward extraction path dominates because the 900,000 mm^{-2} bond density and SiO_2 filling between the SiPh layer and Heat Spreader 1 minimizes $R_{th,up}$. Conversely, the downward path relies on the sparse 10,000 mm_{-2} interface to maximize $R_{th,down}$. Because $R_{th,up} \ll R_{th,down}$, the majority of SiPh heat is efficiently pulled upwards into the package spreaders rather than trapping in the CMOS.

*e) **Steady-State Temperature Budget:**:* Under sustained full-load operation, the steady-state temperature rise of the SiPh layer above ambient is:

$$\Delta T_{SiPh,steady} = P_{tile} \times R_{th,up} \approx 1.5 \times 0.227 \approx 0.34\,^{\circ}\mathrm{C} \tag{147}$$

This is well within the photonic stability envelope. The critical phase-stability threshold for a silicon waveguide of length L = 500 μm is:

$$\Delta T_{crit} = \frac{\lambda \cdot \phi_{max}}{2\pi L \cdot \frac{dn}{dT}} \tag{148}$$

$$= \frac{1.064 \times 10^{-6} \times \pi}{2\pi \times 500 \times 10^{-6} \times 1.86 \times 10^{-4}} \approx 5.7\,^{\circ}\mathrm{C} \tag{149}$$

for a full π-radian phase excursion. The steady-state operating margin is therefore:

TABLE XI
UNIFIED THERMAL PARAMETER SCALING ACROSS JANUS CONFIGURATIONS

Parameter	Symbol	Mini	Edge	Datacenter
Total chip footprint	A_{chip}	40.0 mm^2	100.0 mm^2	300.0 mm^2
Global SiO_2 thickness	h_{SiO_2}	100 μm	100 μm	100 μm
Global SiO_2 heat capacity	C_{SiO_2}	6.2 mJ/K	15.5 mJ/K	46.4 mJ/K
JIR cycle duration	τ_{JIR}	5 μs	5 μs	5 μs
Global worst-case heat/cycle	Q_{gen}	33 μJ	83 μJ	250 μJ
Max. global ΔT/cycle	ΔT_{cyc}	0.0053 °C	0.0054 °C	0.0054 °C
Upward thermal resistance	$R_{\text{th,up}}$	1.38 K/W	0.55 K/W	0.18 K/W
Steady-state SiPh rise	ΔT_{steady}	0.41 °C	0.38 °C	0.32 °C
Phase-drift critical ΔT	ΔT_{crit}	5.7 °C	5.7 °C	5.7 °C
SiO_2 diffusion time	τ_{diff}	11.05 ms	11.05 ms	11.05 ms
HS pillar density (top)	$\rho_{\text{Cu,top}}$	900 k/mm^2	900 k/mm^2	900 k/mm^2
CMOS pillar density (bottom)	$\rho_{\text{Cu,bot}}$	10 k/mm^2	10 k/mm^2	10 k/mm^2

$$Margin = \frac{\Delta T_{crit}}{\Delta T_{SiPh,steady}} \approx \frac{5.7}{0.34} \approx 17\times \tag{150}$$

confirming that the SiPh routing layer remains comfortably inside its phase-stable operating window under all sustained workloads. The large margin directly follows from the increased thermal mass and lower thermal resistance of the 7.5 mm^2 Z-staged tile.

f) ***Vertical Diffusion Time Constant:****:* The time for heat to diffuse vertically through the 100 μm SiO_2 buffer layer, which constitutes the dominant thermal barrier, is:

$$\tau_{diff} = \frac{{h_{SiO_2}}^2}{\alpha_{SiO_2}} \tag{151}$$

where the thermal diffusivity of SiO_2 is:

$$\alpha_{SiO_2} = \frac{k_{SiO_2}}{\rho_{SiO_2} c_{p,SiO_2}} \approx \frac{1.4}{2,200 \times 703} \approx 9.05 \times 10^{-7} m^2/s \tag{152}$$

Therefore:

$$\tau_{\text{diff}} = \frac{(100 \times 10^{-6})^2}{9.05 \times 10^{-7}} \approx 1.105 \times 10^{-2} \text{ s} \tag{153}$$

$$\tau_{\text{diff}} \approx 11.05 \text{ ms} \tag{154}$$

This 11.05 ms vertical diffusion time is more than 2,200 JIR cycles long (τJIR = 5 μs). Consequently, any CMOS-originated thermal transient is completely attenuated by the SiO_2 layer before it can propagate into the SiPh plane on a timescale relevant to optical computation.

The photonic layer occupies a thermodynamic operating region where temperature variation remains bounded within optical stability limits. The permissible phase drift condition is:

$$|\Delta\phi| < \phi_{\text{max}} \tag{155}$$

Substituting the thermal phase relation:

$$|\frac{2\pi L}{\lambda} \frac{dn}{dT} \Delta T| < \phi_{\text{max}} \tag{156}$$

Thus, bounded temperature directly implies bounded routing stability. Because the SiPh layer is thermally insulated from large CMOS thermal fluctuations, the optical network remains inside a stable operating region:

$$H(t) \approx constant \tag{157}$$

throughout sustained operation.

This thermodynamic partition maintains the optical routing substrate within a tightly bounded thermal stability window ($\Delta T \leq 0.048$ K), ensuring that phase determinism is preserved under sustained workloads without requiring active temperature trimming.

5) ***Detector Layer Decoupling****:* Detector arrays are positioned above the photonic routing layer to minimize optical-electrical interference [5], [30]. This vertical placement provides two major advantages :

1) Optical absorption occurs after routing completion, preventing detector thermal dissipation from perturbing upstream waveguides.
2) Detector electrical activity remains physically separated from the sensitive photonic routing mesh.

Thus:

$$C_{\text{detector}\to\text{routing}} \to 0 \tag{158}$$

where: C represents thermoelectrical coupling.

a) ***Interleaved Two-Layer Detector Block Layout:****:* Each photonic tile implements a full N × N matrix–vector multiplication, producing N^2 independent one-hot multiplication results per clock cycle. To read every result, a photodetector must be placed at the terminus of every output waveguide of every multiplier:

$$N_{\text{det}} = N_{\text{tiles}} \times N_{\text{mult/tile}} \times N_{\text{waveguides}} \tag{159}$$

$$= 32 \times 16{,}384 \times 17 = \mathbf{8{,}912{,}896} \tag{160}$$

Although 8,912,896 detectors are physically present across the 17 spatial waveguides ($WG_0 \ldots WG_{16}$), the total active detector count per full 10 ps clock cycle is only $N_{\text{active}} = N_{\text{tiles}} \times N_{\text{dim}}^2 = 524{,}288$, because One-Hot encoding guarantees exactly one waveguide per multiplier carries light. However, to conserve optical master laser power and eliminate an entire

layer of passive splitting, the 10 ps (100 GHz) clock cycle is time-multiplexed into two discrete 5 ps phases. At any instantaneous moment (i.e., within a single 5 ps phase), only half of the photodetectors (262,144) are actively illuminated. This two-phase illumination strategy allows the optical energy to be steered sequentially rather than split simultaneously, functionally doubling the delivered optical power per receiver. Over the full 10 ps cycle, all 524,288 detection events are resolved. The baseline spatial activity ratio $\alpha = 1/17$ reduces dynamic detector power proportionally, as quantified in the power budget (Table XV). The 105 GHz Ge/Si $\mathrm{SAC^2M}$ APD photodetectors occupy approximately $1.5\,\mu\mathrm{m}^2$ per device; 8.91×10^6 detectors require only $\approx 13.37\,\mathrm{mm}^2$ of total detector area within the 300 mm^2 Datacenter die footprint.

To accommodate this high device density without metal wiring bottlenecks, JANUS organizes the photodetector array into an interleaved two-layer detector block. Each detector block consists of two vertically stacked Ge/Si $\mathrm{SAC^2M}$ APD sub-arrays, each handling alternating odd and even waveguide channels, addressed through separate metal interconnect layers. This interleaved arrangement halves the required wiring pitch per layer, suppresses inter-detector electrical crosstalk, and improves the spatial uniformity of the thermal dissipation profile directly below the primary heat spreader (HS1). The two-layer structure is fabricated within the same backend module as the SiPh routing stack and preserves detector margin consistency under sustained high-throughput operation.

*6) **Event-Driven Dynamic Latched Readout**:* Scaling to 8.91×10^6 physical detectors requires extreme mitigation of static power dissipation. Conventional continuous-time transimpedance amplifiers (TIAs) consume unacceptable milliwatt-level static power per channel [48], which would fundamentally break the thermodynamic scaling limit of the chip. To resolve this, JANUS eschews continuous linear readout in favor of an *event-driven dynamic latched comparator* architecture (e.g., clocked StrongARM latches) integrated intimately with the Ge/Si APDs [49], [50].

This topology trades continuous analog linearity for ultra-low-power binary sensing [51], [52]. Dynamic regenerative latches consume essentially zero static power; dynamic power is consumed exclusively during state transitions triggered by a clock edge and an incoming photon pulse. Because JANUS operates on a strictly sparse One-Hot arithmetic basis, only 1 in 17 waveguides is optically active per cycle ($\alpha = 1/17$). Hierarchical wake-up gating ensures that the vast majority of latches remain asleep, and only the optically triggered channels resolve. Combining highly scaled integration (parasitic input capacitance $C_{\text{int}} \leq 3$ fF) [53] with column-shared sample-and-hold (S/H) multiplexing [54] amortizes the already low per-decision latch energy ($\approx$ 10–100 fJ) down to an effective electrical cost of $\approx$ 100 aJ (0.1 fJ) per active detection. As formalized in Table XV, this bounds the Datacenter detector dynamic power to a highly manageable 5.24 W, avoiding the thermal scaling wall inherent to continuous TIA arrays.

*7) **Mechanical and Fabrication Implications**:* The layered stack additionally improves fabrication modularity. Each subsystem can be optimized independently:

- CMOS for logic density,
- SiPh for low-loss routing,
- detectors for responsivity and bandwidth.

Thus, no single fabrication process must simultaneously optimize all electrical, optical, thermal, and nonlinear properties.

This modularity substantially improves manufacturability relative to monolithic heterogeneous photonic integration.

*8) **Thermal Scaling Across Configurations**:* Thermal stability is preserved across all JANUS deployment scales because optical routing density remains vertically isolated from the dominant CMOS heat plane. Importantly, thermal behavior does not catastrophically degrade with routing scale because the dominant heat paths remain directionally partitioned.

TABLE XII
THERMAL STABILITY SCALING ACROSS JANUS CONFIGURATIONS

Metric	Mini	Edge	Datacenter
SiPh Routing Strata	3	4	5
Active Stack Height	250 μm	280 μm	310 μm
Total Package Height	$\approx$ 0.58 mm	$\approx$ 0.61 mm	$\approx$ 0.64 mm
SiO_2 Thermal Buffer	100 μm	100 μm	100 μm
CMOS Thermal Coupling	Minimal	Minimal	Minimal
Optical Phase Drift	Bounded	Bounded	Bounded
Calibration Stability	Stable	Stable	Stable
Thermal Equilibrium	Maintained	Maintained	Maintained

*9) **Architectural Consequences**:* The 3D Z-axis stack fundamentally changes the thermodynamic behavior of large-scale photonic systems.

1) Optical routing becomes thermally isolated from CMOS activity.
2) Phase drift remains bounded within stable operating limits.
3) Calibration overhead collapses because the transfer matrix remains approximately stationary.
4) Passive routing strata, photodetector arrays, and CMOS digital logic each occupy vertically partitioned, thermally decoupled physical planes.
5) Finally, the architecture achieves sustained thermodynamic equilibrium under high-throughput operation.

Thus, JANUS does not merely cool a photonic accelerator. It reorganizes the entire computational stack around directional thermal stability.

IV. SYSTEM -LEVEL SCALING ANALYSIS

A. Constraint-Bounded Scaling Philosophy

Conventional accelerator architectures often evaluate scalability using peak theoretical throughput alone. Such methodology is fundamentally misleading for photonic systems because large-scale operation is dominated not by arithmetic density, but by the interaction between thermal, optical, informational, and nonlinear constraints.

JANUS instead adopts a bounded scaling philosophy:

Scalability $\equiv$ Ability to Remain Physically Stable Under Growth

Thus, every scaling dimension must remain bounded simultaneously:

$$P_{noise} < P_{signal} < P_{sat}$$

$$T_{junction} < T_{critical}$$

$$\phi_{\text{drift}} < \phi_{\text{max}}$$

$$P_{undetected} \to 0$$

Only architectures satisfying all four constraints simultaneously can sustain exact arithmetic at large scale.

B. *Spatial Scaling Characteristics*

Unlike conventional analog photonic accelerators, JANUS scales primarily through spatial parallelism.

Throughput scales as:

$$\text{T} \propto \text{N}_{\text{tiles}}$$

where: N_{tiles} is the number of independent optical residue tiles.

Importantly, local optical precision remains bounded regardless of system scale:

$$\text{P}_{local} = \text{constant}$$

Thus, global arithmetic precision increases through modular composition rather than increasing analog signal fidelity. This fundamentally differs from conventional analog systems, where precision scaling requires exponentially increasing SNR.

The resulting architecture obeys:

$$\text{Global Precision} \propto N_{\text{tiles}}$$

while:

$$\text{Local Analog Complexity} \approx \text{constant}$$

This bounded-local-complexity principle is central to the scalability of JANUS.

C. *Routing Complexity Scaling*

The routing complexity of the JANUS Asymmetric 16-Tree Fermat Core scales as:

$$O(M \log M) \text{ with } M = 16$$

rather than $O(M^2)$ for conventional crossbars or $O(N_{\text{alphabet}} \log N_{\text{alphabet}})$ across unreduced permutation meshes. Exploiting One-Hot spatial sparsity—wherein only one waveguide is active per residue multiplication—each active waveguide $(WG_1 \dots WG_{16})$ routes through an independent 4-stage binary tree:

$$S_{16\text{-tree}} = \log_2(16) = 4 \text{ stages (universal)} \tag{161}$$

Thus, across all three deployment configurations:

$$\mathbf{S}_{Mini} = \mathbf{S}_{Edge} = \mathbf{S}_{Datacenter} = \mathbf{4}$$

establishing an ultra-shallow optical routing depth of $S_{16\text{-tree}} = 4$. Importantly, routing depth remains strictly constant across all matrix dimensions N.

Consequently, optical loss accumulation across the routing fabric is restricted to just $1.61\,\text{dB}$ across 4 stages, guaranteeing robust passive fan-out closure with Ge/Si APD detection without intermediate optical amplification.

D. *Optical Power Equilibrium*

Large-scale photonic systems commonly fail because optical power either:

1) decays below detector thresholds,
2) or increases into nonlinear saturation regimes.

JANUS instead operates within a bounded optical equilibrium region:

$$P_{noise} < P_{signal} < P_{sat}$$

Instead of relying on intermediate optical amplification, JANUS ensures that the delivered optical power ($P_{\text{det}} \approx -18.59\,\text{dBm}$) exceeds the practical sensitivity threshold of the Ge/Si APD receivers ($P_{\text{sens,practical}} \approx -23.20\,\text{dBm}$) by $+4.61\,\text{dB}$ across all routing depths:

$$P_{\text{det}} > P_{\text{sens,practical}}$$

Thus, throughout propagation from launch to detection, the signal intensity remains strictly within the bounded optical equilibrium window without requiring intermediate gain compensation.

Because the architecture uses only a single optical wavelength, nonlinear spectral interactions remain structurally suppressed. Therefore, optical equilibrium persists even under large fanout scales.

E. *Thermal Scaling Characteristics*

Thermal stability is maintained through directional Z-axis heat routing.

CMOS thermal dissipation preferentially propagates downward:

$$q_{CMOS} \downarrow$$

while photonic and detector thermal dissipation preferen tially propagates upward:

$$q_{photonic} \uparrow$$

The intermediate dielectric and buffer layer suppresses thermal coupling:

$$\frac{\partial T_{SiPh}}{partial T_{CMOS}} \to 0$$

Thus, optical phase stability remains approximately invariant under increasing digital activity.

Importantly, the photonic routing layer remains within a bounded thermodynamic region even as total system throughput increases.

F. *Fault Visibility Scaling*

Conventional approximate systems become less observable at larger scale because fault complexity grows faster than monitoring capability. JANUS exhibits the opposite behavior.

CRT reconstruction amplifies local residue faults into globally invalid arithmetic states:

$$|X' - X| \gg |\delta|$$

Thus, larger CRT dynamic ranges increase fault visibility rather than decreasing it. The probability of silent undetected corruption therefore approaches:

TABLE XIII
SYSTEM-LEVEL ROUTING SCALING ACROSS JANUS CONFIGURATIONS

Metric	Mini (32 Tiles)	Edge (32 Tiles)	Datacenter (32 Tiles)
Tile Matrix Dimension	32×32	64×64	128×128
Total Multipliers	32,768	131,072	524,288
16-Tree Routing Stages (S)	4	4	4
Switches per Multiplier Core	**240**	**240**	**240**
Total Fabric Routing Switches	**7,864,320**	**31,457,280**	**125,829,120**
Fabric Routing Insertion Loss	**1.61** dB	**1.61** dB	**1.61** dB
Static Routing Hold Power	**0.00** W (PCM Non-Volatile)	**0.00** W (PCM Non-Volatile)	**0.00** W (PCM Non-Volatile)
Passive Fan-Out Optical Link Closure	**Verified** (+10.50 dB Margin)	**Verified** (+7.50 dB Margin)	**Verified** (+4.61 dB Margin)

$$P_{silent} \to 0$$

under bounded fault assumptions.

This property is especially important for exact arithmetic workloads where approximate degradation is unacceptable.

G. Bandwidth Scaling Characteristics

Because JANUS scales spatially rather than spectrally, throughput growth does not require increased wavelength density.

Conventional DWDM systems obey:

$$T \propto N_\lambda$$

which increases nonlinear spectral interaction complexity.

JANUS instead obeys:

$$T \propto N_{spatial}$$

Thus, throughput increases through physically independent routing channels.

Consequently:

$$\frac{\partial C_i}{\partial C_j} \approx 0 (i \neq j)$$

and inter-channel entropy propagation remains bounded.

This distinction prevents the nonlinear instability escalation observed in conventional spectrally multiplexed photonic systems.

H. Energy Scaling Behavior

The total energy consumption of JANUS is dominated by:

$$E_{total} = E_{CMOS} + E_{laser} + E_{detector} + E_{reconfiguration}$$

Importantly, routing hold power disappears because PCM switches are non-volatile:

$$P_{hold} \approx 0$$

Thus, routing energy scales with reconfiguration frequency rather than routing size. This substantially improves asymptotic thermal behavior compared with thermo-optic architectures.

I. System Power Budget

The total system power of JANUS is decomposed by functional layer. Because PCM routing switches are non-volatile, their static hold power is approximately zero under infrequent-reconfiguration workloads. Table XV provides the full breakdown for all three deployment configurations under sustained full-load operation.

For reference, a thermally tuned equivalent system using conventional thermo-optic MZI heaters at the typical 0.10 mW per switch would require:

$$P_{heaters,conv} = N_{switch} \times 0.10mW \tag{162}$$

For the Datacenter configuration with $N_{\text{switch}} = 125,829,120$ PCM switches (240 switches per multiplier across $524,288$ multipliers):

$$P_{\text{heaters,conv}} = 125,829,120 \times 0.10 \times 10^{-3} = 12.58\,\text{kW} \tag{163}$$

By replacing thermo-optic MZIs with non-volatile PCM routing, JANUS achieves a static routing power reduction from over 12.58 kW to identically zero (0.00 W) across the entire Datacenter tier, eliminating the multi-kilowatt static thermal burden inherent to continuously biased interferometric meshes.

J. Peak and Sustained Throughput Derivation and RNS Precision Scaling

a) Wave-Pipelined Operating Frequency Derivation:: In the JANUS wave-pipelined architecture, functional stages along the optical-to-electrical datapath are physically decoupled in space, operating concurrently on successive in-flight optical pulses. Consequently, the minimum clock cycle period T_{cycle} is not the cumulative sum of stage latencies, but is bounded by the bottleneck single-stage processing and recovery duration:

$$T_{\text{cycle}} = \max\left(t_{\text{mod}}, t_{\text{PD}}, t_{\text{wire}}, t_{\text{guard}}\right) \leq 10.0\,\text{ps} \tag{164}$$

Each concurrent stage satisfies the 10.0 ps timing boundary:

1) **Electro-Optic Injection Interval ($t_{\text{mod}} \leq 10.0$ ps):** The $LiTaO_3$ Pockels-effect input router formats and injects optical pulses with full-width half-maximum $\tau_{\text{FWHM}} \approx$

TABLE XIV
SYSTEM-LEVEL STABILITY CHARACTERISTICS ACROSS JANUS CONFIGURATIONS

Metric	Mini	Edge	Datacenter
Per-Tile Residue Channel Width	8-bit ($m_i \leq 256$)	8-bit ($m_i \leq 256$)	8-bit ($m_i \leq 256$)
Single-Tile Operand Precision ($k = 1$)	4-bit (INT4)	4-bit (INT4)	4-bit (INT4)
Global Precision Scaling	Spatial	Spatial	Spatial
Spectral Channels	1	1	1
Optical Equilibrium	Maintained	Maintained	Maintained
Thermal Stability	Bounded	Bounded	Bounded
Fault Visibility	High	High	High
Static Routing Hold Power	0 W	0 W	0 W
Silent Arithmetic Corruption	Suppressed	Suppressed	Suppressed

TABLE XV
JANUS FULL-SYSTEM POWER BUDGET BY COMPONENT LAYER. PCM ROUTING SWITCHES CONTRIBUTE 0 W STATIC HOLD POWER. ALL VALUES ARE PEAK SUSTAINED ESTIMATES AT 100 GHz OPERATION.

Component Layer	Mini	Edge	Datacenter
1064 nm Yb Laser (75% WPE)	≈ 6.67 W	≈ 26.67 W	≈ 133.33 W
LiTaO3 Pockels Ring Routers	1.02 W	4.10 W	8.19 W
Ge/Si APD Detectors ($M = 7$)	0.33 W	1.31 W	5.24 W†
Optical Amplification Layer	0 W	0 W	0 W
PCM Routing Switches (static)	0.00 W	0.00 W	0.00 W
CMOS (Encoders / Adders / CRT)	2.01 W	8.50 W	37.03 W
JIR Scheduler and Control Logic	3.00 W	3.00 W	3.00 W

†Assumes highly amortized event-driven S/H readout ($\approx$ 100 aJ per active detection).

3–5 ps into the active One-Hot waveguide at a 10.0 ps repetition interval.

2) **Photodetector Carrier Clearance ($t_{\text{PD}} \approx 1.52$ ps):**

$$t_{\text{PD}} = \frac{1}{2\pi \cdot f_{\text{3dB}}} = \frac{1}{2\pi \times 105\,\text{GHz}} \approx 1.52\,\text{ps}$$

where the 105 GHz receiver bandwidth corresponds to the high-speed Ge/Si SAC^2M avalanche photodetectors [5]. Photogenerated carriers clear the multiplication region in ≈ 1.52 ps, ensuring complete reset well before the next pulse arrives in the 10.0 ps slot.

3) **Electrical Interconnect Delay ($t_{\text{wire}} \approx 1.33$ ps):** Local on-chip wire propagation over a 200 μm effective metal path ($v \approx 1.5 \times 10^8$ m/s) requires:

$$t_{\text{wire}} = \frac{200 \times 10^{-6}}{1.5 \times 10^8} \approx 1.33\,\text{ps}$$

4) **Inter-Pulse Guard Margin ($t_{\text{guard}} \approx 3.5$ ps):** Provides temporal isolation between adjacent in-flight optical wavefronts to prevent inter-symbol interference (ISI) and group velocity dispersion across the passive routing fabric.

Thus, the sustained system operating clock frequency is:

$$f_{\text{clk}} = \frac{1}{T_{\text{cycle}}} = \frac{1}{10.0\,\text{ps}} = 100\,\text{GHz} \tag{165}$$

*b) **Pipelining and End-to-End Latency Clarification:**:* The 10.0 ps cycle time represents the throughput interval (the time between successive optical pulses entering the routing fabric), not the end-to-end latency of a single computation. The cumulative single-computation end-to-end latency consists of:

1) **PCM 16-Tree Fermat Core optical propagation:** The 4 routing stages ($\log_2 16 = 4$) have an ultrafast optical propagation latency of only $t_{\text{opt}} \approx 1.33$ ps across the compact binary tree fabric (measured in full-wave simulation). Because the non-volatile PCM states remain static throughout an inference epoch, successive optical pulses stream through the fabric every 10.0 ps in a wave-pipelined fashion.
2) **CMOS CRT adder-tree accumulation:** The CMOS backend accumulates and reconstructs residues with an optimized 8-stage pipelined adder-tree latency of approximately $t_{\text{CRT}} \approx 80.0$ ps (at 10.0 ps per register stage, reduced from 210 ps). This latency is hidden behind deeply staged CMOS registers that process reconstruction in parallel with optical transport.

The cumulative single-computation end-to-end latency is approximately:

$$T_{\text{latency}} \approx t_{\text{opt}} + t_{\text{PD}} + t_{\text{wire}} + t_{\text{CRT}} \approx 1.33 + 1.52 + 1.33 + 80.0 \approx 84.18\,\text{ps} < 10 \tag{166}$$

from initial pulse injection to final reconstructed word, achieving an ultrafast end-to-end latency and collapsing the required wave-pipelined queue depth down to only 8–9 in-flight computation stages at 100 GHz.

*c) **Per-Tile Raw MAC Rate:**:* Each photonic tile implements an $N \times N$ matrix–vector multiplication in one optical clock cycle. The raw per-tile multiply-accumulate rate is:

$$\dot{M}_{\text{tile}} = N^2 \times f_{\text{clk}} \tag{167}$$

For the three JANUS deployment configurations:

$$\dot{M}_{\text{Mini,tile}} = 32^2 \times 100\,\text{GHz} = 102.4\,\text{TMAC/s} \tag{168}$$

$$\dot{M}_{\text{Edge,tile}} = 64^2 \times 100\,\text{GHz} = 409.6\,\text{TMAC/s} \tag{169}$$

$$\dot{M}_{\text{DC,tile}} = 128^2 \times 100\,\text{GHz} = 1,638.4\,\text{TMAC/s} \tag{170}$$

*d) **Sustained Utilization Factor:**:* Not all tile cycles correspond to valid computation. The JIR scheduler maintains tiles in a warm-dominant regime, with controlled transitions to Hot state for active computation. The sustained utilization factor is derived from the thermal duty-cycle analysis of Section III-G:

$$\eta = 0.85$$

This factor accounts for:

- JIR state-transition overhead ($\approx 4\ \mu$s per rotation cycle),
- PCM reconfiguration cycles (sparse, $\ll 1\%$ overhead under sustained inference),
- CRT reconstruction pipeline flushing (contained within the τJIR = 5 μs cycle, introducing no per-operation stall).

***Simultaneous Weight Loading and Zero-Overhead Reconfiguration**:* PCM reconfiguration introduces far less than 1% overhead because the JANUS architecture reprograms switches in parallel rather than sequentially. The entire weight fabric—up to $125,829,120$ non-volatile PCM switches in the Datacenter configuration (240 switches per multiplier across $524,288$ multipliers)—can, in principle, be reprogrammed in a single 0.1 ms window using electro-thermal micro-heaters integrated directly within the phase-change switch cells. During the weight-loading window, the underlying CMOS driver layer asserts parallel electrical programming current pulses across the 32 tile driver matrices via the vertical Cu–Cu interconnect grid. This electro-thermal addressing scheme delivers the required 10–50 pJ programming energy (SET/RESET) per switch without requiring any auxiliary optical write lasers or complex optical pump distribution networks.

Furthermore, the 0.1 ms weight-loading window is not idle for the CMOS backend. The accumulated CRT reconstruction backlog from the previous compute epoch is processed during this interval. Because the CMOS pipeline is deeply staged, the reconstruction of the final batch of optical results from the previous epoch overlaps entirely with the electrical programming pulse cycle, yielding zero effective CMOS stall overhead attributable to reconfiguration. The net system utilization therefore remains at $\eta = 0.85$ rather than degrading with model-weight update frequency.

***Reconfiguration Energy Budget**:* PCM state transitions require write energy E_{PCM} per switch, which varies with device geometry, active volume, and the crystallisation (SET) versus amorphisation (RESET) direction. For plasmonic PCM switches of the type employed in JANUS, three design tiers bound the operating envelope across $N_{\text{sw}} = 125,829,120$ switches ($\approx 1.258 \times 10^8$ switches):

- **Tier 1 (highly optimised, ≈100 fJ):** Sub-wavelength MIM plasmonic structures, primarily crystallisation pulses.

$$E^{T1}{}_{\text{reconfig}} = 1.258 \times 10^8 \times 100 \times 10^{-15} \approx 12.58\,\mu\text{J} \quad (171)$$

$$P^{T1}{}_{\text{transient}} = \frac{12.58\,\mu\text{J}}{0.1\,\text{ms}} \approx 0.126\,\text{W} \quad (172)$$

- **Tier 2 (balanced neuromorphic, ≈1 pJ):** Mixed SET/RESET operations across a standard plasmonic array.

$$E^{T2}{}_{\text{reconfig}} = 1.258 \times 10^8 \times 1 \times 10^{-12} \approx 0.126\,\text{mJ} \quad (173)$$

$$P^{T2}{}_{\text{transient}} = \frac{0.126\,\text{mJ}}{0.1\,\text{ms}} \approx 1.26\,\text{W} \quad (174)$$

- **Tier 3 (conservative upper bound, ≈10 pJ):** Larger active volumes, unoptimised thermal leakage, or consecutive high-energy RESET pulses.

$$E^{T3}{}_{\text{reconfig}} = 1.258 \times 10^8 \times 10 \times 10^{-12} \approx 1.26\,\text{mJ} \quad (175)$$

$$P^{T3}{}_{\text{transient}} = \frac{1.26\,\text{mJ}}{0.1\,\text{ms}} \approx 12.6\,\text{W} \quad (176)$$

Even under the conservative Tier 3 scenario, the total transient electrical programming power dissipation across the entire chip reaches only 12.6 W during the 0.1 ms write window. Distributing this transient electrical load across the 300 mm^2 Datacenter die through the 32 spatially partitioned CMOS tile driver arrays yields an exceptionally benign peak transient power density of ≈ 0.042 W/mm^2, which is well within the thermal extraction capability of the perimeter thermal shunt and remains far below the ~ 1 W/mm^2 limit demonstrated in high-performance silicon flip-chip packages. After the write window closes, the PCM state is latched non-volatilely and the transient power returns to zero; no sustained thermal load is imposed on the optical stack. In the operationally dominant mode—incremental reconfiguration updating only the fraction f_Δ of changed weights between inference epochs—the energy scales as $E_\Delta = f_\Delta \times E_{\text{reconfig}}$. For typical sparse fine-tuning updates ($f_\Delta < 1\%$), Tier 3 reduces to $< 13\,\mu$J per update, making reconfiguration energy negligible relative to inference throughput. Full simultaneous weight loading across all switches is therefore characterized as an "in-principle" upper bound; operational reprogramming exploits incremental weight sparsity via the partitioned CMOS driver arrays.

*e) **Peak Theoretical Throughput** ($\eta = 1.0$):* The peak theoretical throughput of the architecture represents the raw hardware computational capacity when all N_{tiles} and optical multipliers operate concurrently at $f_{\text{clk}} = 100$ GHz under 100% utilization ($\eta = 1.0$):

$$\dot{M}_{\text{peak}} = N_{\text{tiles}} \times \dot{M}_{\text{tile}} = N_{\text{tiles}} \times N_{\text{dim}}^2 \times f_{\text{clk}} \quad (177)$$

For single-tile direct operation ($P = 4$, $k = 1$):

$$\dot{M}_{\text{peak,Mini}} = 32 \times 32^2 \times 100\ \text{GHz} = 3,276.8\ \text{TMAC/s} \quad (178)$$

$$\dot{M}_{\text{peak,Edge}} = 32 \times 64^2 \times 100\ \text{GHz} = 13,107.2\ \text{TMAC/s} \quad (179)$$

$$\dot{M}_{\text{peak,DC}} = 32 \times 128^2 \times 100\ \text{GHz} = 52,428.8\ \text{TMAC/s} \quad (180)$$

*f) **Sustained Operational Throughput** ($\eta = 0.85$):* Accounting for JIR scheduling, thermal rotation, and CRT reconstruction pipeline flushing ($\eta = 0.85$), the sustained operational throughput is:

$$\dot{M}_{\text{sust}} = \eta \times \dot{M}_{\text{peak}} \tag{181}$$

Thus, at single-tile direct operation ($P = 4$, $k = 1$):

$$\dot{M}_{\text{sust,Mini}} = 0.85 \times 3,276.8 \text{ TMAC/s} \approx 2,785.3 \text{ TMAC/s} \tag{182}$$

$$\dot{M}_{\text{sust,Edge}} = 0.85 \times 13,107.2 \text{ TMAC/s} \approx 11,141.1 \text{ TMAC/s} \tag{183}$$

$$\dot{M}_{\text{sust,DC}} = 0.85 \times 52,428.8 \text{ TMAC/s} \approx 44,564.5 \text{ TMAC/s} \tag{184}$$

*g) **Precision Scaling via Spatial RNS** ($P \geq 8$, $k \geq 2$):* Each optical tile implements a modular residue channel of width $\log_2(256) = 8$ bits ($m_i \leq 256$). When multiplying two wide integers of operand width P bits, the resulting product spans $2P$ bits of dynamic range. To reconstruct this product without modular ambiguity, the computation is partitioned across k independent 8-bit residue tiles:

$$k = \left\lceil \frac{2P}{8} \right\rceil = \left\lceil \frac{P}{4} \right\rceil \tag{185}$$

optical tiles allocated in parallel.

Thus:

$$k_{\text{INT4 }(P=4)} = 1, \quad k_{\text{INT8 }(P=8)} = 2, \quad k_{\text{INT16 }(P=16)} = 4,$$
$$k_{\text{INT32 }(P=32)} = 8, \quad k_{\text{INT64 }(P=64)} = 16$$

The precision-scaled peak and sustained throughput scale inversely with k:

$$\dot{M}_{\text{peak}}(P) = \frac{\dot{M}_{\text{peak,INT4}}}{k}, \qquad \dot{M}_{\text{sust}}(P) = \frac{\dot{M}_{\text{sust,INT4}}}{k} \tag{186}$$

This linear inverse scaling in k represents the exact cost of achieving higher arithmetic precision through spatial modular composition. For 64-bit precision ($k = 16$), the 16 allocated tiles operate under Hybrid Partitioning, splitting the operands into 32-bit halves. The tiles compute the direct sub-products ($X_L \cdot Y_L$ and $X_H \cdot Y_H$) fully optically in two 8-tile clusters, while the massive cross-term ($X_L Y_H + X_H Y_L$) is offloaded entirely to CMOS SRAM Memory Lookup Tables (LUTs). This resolves the full 64-bit matrix multiplication without modular overflow. No analog signal quality or dynamic range is sacrificed; the tradeoff is purely in physical tile allocation and CMOS integration.

*h) **Energy Efficiency at 64-bit Precision**:*

$$\eta_{EE} = \frac{\dot{M}_{\text{sust}}(\text{64-bit})}{P_{\text{total}}} \tag{187}$$

For the three configurations:

$$\eta_{EE,Mini} = \frac{174.1 \text{ TMAC/s}}{13.03 \text{ W}} \approx 13.36 \text{ TMAC/s/W} \tag{188}$$

$$\eta_{EE,Edge} = \frac{696.3 \text{ TMAC/s}}{43.58 \text{ W}} \approx 15.98 \text{ TMAC/s/W} \tag{189}$$

$$\eta_{EE,DC} = \frac{2,785.3 \text{ TMAC/s}}{186.79 \text{ W}} \approx 14.91 \text{ TMAC/s/W} \tag{190}$$

*i) **Comprehensive Performance Profile Summary**:* Tables XIX, XX, and XXI (consolidated in Appendix G) present the complete peak theoretical and sustained operational throughput scaling, along with energy efficiency figures, across all three JANUS deployment configurations (Mini, Edge, and Datacenter) and target integer precisions (INT4 through INT64). All values represent exact integer operations without analog approximation.

K. Asymptotic Architectural Implications

The scaling behavior of JANUS differs fundamentally from conventional analog photonic accelerators. Conventional architectures exhibit:

Higher Scale → Higher Instability

because thermal drift, nonlinear interaction, calibration overhead, analog precision requirements, and fault observability all worsen with growth. JANUS instead enforces bounded local operating conditions while scaling globally through modular spatial composition.

Higher Scale → Higher Parrallelism

without proportionally increasing local physical instability. This bounded-local-state principle is the primary architectural reason why JANUS remains physically scalable under exact arithmetic workloads.

V. Physical Feasibility and Constraint Compliance

A. Constraint-First Validation Philosophy

The validity of JANUS does not emerge from peak theoretical throughput claims alone. Instead, feasibility is determined by whether every subsystem remains consistent with known thermodynamic, optical, informational, and electrical constraints.

Therefore, each architectural mechanism must satisfy four conditions simultaneously:

1) Physical Realizability
2) Thermodynamic Stability
3) Bounded Error Propagation
4) Sustained Operational Equilibrium

Any subsystem violating one of these conditions becomes physically non-scalable regardless of theoretical arithmetic density.

Accordingly, JANUS was derived through iterative elimination of architectures that failed under one or more physical constraints. The resulting system therefore represents a constraint satisfying architecture rather than a performance-maximized approximation.

B. Shannon Capacity Compliance

The primary failure mode of conventional analog photonic accelerators is violation of Shannon-limited information recoverability. For a communication channel with bandwidth: B and signal-to-noise ratio SNR the maximum recoverable information rate is:

$$\mathrm{C} = \mathrm{B}\ log_2(1 + SNR)$$

Conventional analog optical accumulation attempts to reconstruct large integer values directly from optical amplitude. As previously derived, exact accumulation requires effective analog SNR approaching:

$$\mathrm{SNR}_{Mini} \approx 126.4 \text{ dB}$$

$$\mathrm{SNR}_{Edge} \approx 132.4 \text{ dB}$$

$$\mathrm{SNR}_{Datacenter} \approx 138.4 \text{ dB}$$

Such requirements exceed realistic detector capability at 100 GHz operating frequencies. JANUS resolves this contradiction by reformulating arithmetic into binary spatial localization. The detector condition reduces to:

$$\mathrm{P}_{signal} > \mathrm{P}_{noise}$$

which corresponds approximately to:

$$\mathrm{SNR} > 0 \text{ dB}$$

Thus, JANUS remains consistent with Shannon information bounds because it no longer attempts exponentially precise analog amplitude recovery. Instead, information is encoded spatially through deterministic One-Hot routing.

TABLE XVI
SHANNON COMPLIANCE COMPARISON BETWEEN ANALOG AND JANUS ARCHITECTURES

Metric	Mini	Edge	Datacenter
SNR Requirement	126.4 dB	132.4 dB	138.4 dB
Spatial Detection SNR	> 0 dB	> 0 dB	> 0 dB
Detection Type	Binary	Binary	Binary
ADC Requirement	Eliminated	Eliminated	Eliminated
Shannon Feasibility	Bounded	Bounded	Bounded

C. Thermodynamic Compliance

Large-scale photonic systems commonly violate thermodynamic feasibility through excessive static routing power density. For thermo-optic MZI routing:

$$\mathrm{P}_{hold} = \mathrm{N}_{switch} \times P_{MZI}$$

with:

$$\mathrm{P}_{MZI} \approx 0.10 \text{ mW}$$

The resulting static thermal loads become:

$$\mathrm{P}_{\mathrm{Mini,TO}} = 786.4 \text{ W}$$

$$\mathrm{P}_{\mathrm{Edge,TO}} = 3.15 \text{ kW}$$

$$\mathrm{P}_{\mathrm{Datacenter,TO}} = 12.58 \text{ kW}$$

Such heat densities exceed realistic chip-scale thermal extraction limits. JANUS eliminates this failure mechanism through non-volatile PCM switches. After programming:

$$\mathrm{P}_{hold} \approx 0 \text{ W}$$

Thus, routing power scales with reconfiguration frequency rather than switch count. Additionally, thermal isolation is enforced through directional Z-axis heat partitioning:

$$\frac{\partial T_{SiPh}}{\partial T_{CMOS}} \to 0$$

This prevents optical routing drift caused by CMOS thermal activity. Consequently, JANUS remains thermodynamically bounded under sustained operation.

D. Nonlinear Optical Compliance

Conventional DWDM photonic systems violate nonlinear optical stability at high channel density due to Kerr-induced spectral mixing. The nonlinear refractive response becomes:

$$\mathrm{n} = \mathrm{n}_0 + \mathrm{n}_2\mathrm{I}$$

which produces Four-Wave Mixing:

$$\omega_{FWM} = \omega_1 + \omega_2 - \omega_3$$

The resulting nonlinear interference scales approximately as:

$$P_{NL} \propto \gamma P^3 L^2$$

Thus, higher wavelength density eventually increases spectral corruption. JANUS eliminates this failure mechanism structurally by enforcing:

$$\mathrm{N}_\lambda = 1$$

Without multiple carrier frequencies, inter-channel spectral mixing cannot occur. Therefore:

$$P_{ghost} \to 0$$

under bounded operating conditions. This architecture remains consistent with nonlinear optical stability limits because nonlinear spectral interaction mechanisms are absent.

E. Amplification Noise Compliance

Conventional SOAs violate exact arithmetic recoverability because gain introduces amplified spontaneous emission noise:

$$\sigma^2{}_{ASE} \propto G n_{sp} B$$

Thus:

$$SNR_{out} < SNR_{in}$$

under conventional amplification.

JANUS eliminates this failure mechanism entirely by removing all intermediate optical amplifiers from the signal path. Instead, a high-power 1064 nm Yb-fiber master laser scales its optical launch power to balance the passive splitting loss of each specific configuration ($P_{\text{laser}} \approx 5\,\text{W}$ for Mini, 20 W for Edge, and 100 W for Datacenter, with WPE > 75%). This targeted power scaling ensures the optical signal survives the respective passive fan-out and routing losses, delivering

$P_{\text{det}} \geq -18.95\,\text{dBm}$ at each detector. Crucially, this provides a strictly uniform $\approx +4.25$ to $+4.85\,\text{dB}$ safety margin over the practical $-23.20\,\text{dBm}$ APD sensitivity threshold across all three deployment scales. Detection employs Ge/Si SAC^2M avalanche photodetectors operating at moderate gain $M = 7$ with an effective ionisation ratio $k \approx 0.06$, yielding an excess noise factor $F(M) \approx 2.0$—far below conventional InGaAs APDs. The resulting noise penalty is bounded and deterministic:

$$\text{F}_{APD}(\text{M = 7}) \approx 2.0$$

Because no gain medium is present in the optical path, ASE noise is structurally absent:

$$\sigma^2{}_{ASE} = 0$$

Thus, JANUS satisfies bounded optical equilibrium conditions by eliminating the amplification noise source entirely rather than attempting to suppress it.

F. *Fault Detectability Compliance*

Conventional approximate systems permit silent arithmetic corruption. Under graceful degradation:

$$\text{X} \rightarrow \text{X} + \epsilon$$

small faults remain numerically plausible. JANUS instead enforces arithmetic invalidation through CRT inconsistency amplification. A residue fault:

$$x_j \rightarrow x_j + \delta$$

produces reconstructed deviation:

$$X' = X + \delta M_j N_j \mod M$$

Thus:

$$|X' - X| \gg |\delta|$$

rendering local residue corruptions globally detectable and distinct from valid range values.

The probability of silent undetected corruption therefore approaches:

$$\text{P}_{silent} \rightarrow 0$$

under bounded fault assumptions. This behavior satisfies deterministic exact arithmetic visibility requirements absent in conventional approximate architectures.

G. *Calibration Stability Compliance*

Large interferometric photonic meshes often require continuous dynamic calibration due to thermal phase drift:

$$\Delta\phi = \frac{2\pi L}{\lambda}\frac{dn}{dT}\Delta T \tag{191}$$

In conventional architectures:

$$H(t) \neq H(t + \Delta t)$$

Thus, routing correctness continuously evolves over time. JANUS suppresses this instability through:

1) Non-volatile PCM routing,
2) Thermal Z-axis partitioning,
3) Single-wavelength operation,
4) Bounded optical equilibrium.

Consequently:

$$\text{H(t)} \approx \text{constant}$$

under sustained operating conditions. Therefore, the architecture avoids the runaway calibration overhead commonly observed in large interferometric meshes.

H. *Physical Constraint Summary*

The architectural validity of JANUS emerges from simultaneous compliance with governing physical, optical, and thermodynamic constraints. Each subsystem is systematically structured to operate within sustainable physical boundary conditions under large-scale spatial integration.

I. *Feasibility Interpretation*

JANUS does not claim violation of physical limits. Instead, it explicitly reorganizes computation to remain inside them.

The architecture avoids:

- exponential analog precision scaling,
- unbounded thermal density,
- spectral nonlinear instability,
- unrecoverable amplification entropy,
- silent arithmetic degradation.

This distinction is critical. Many photonic accelerator proposals attempt to overpower physical constraints through additional calibration, higher laser power, or more aggressive analog reconstruction. JANUS instead reformulates the computational problem itself so that the constraints become structurally bounded. Consequently, scalability emerges not from violating physical laws, but from remaining consistent with them.

VI. DISCUSSION

A. *Reframing the Objective of Photonic Computation*

Most photonic accelerator research attempts to maximize arithmetic density by directly emulating conventional electronic matrix multiplication in the optical domain [3], [19], [40], [55]. This approach implicitly assumes that optical systems can scale analog precision similarly to digital electronics.

However, the preceding analysis demonstrates that this assumption fails under large-scale exact arithmetic workloads. Thermal drift, optical shot noise, ADC precision limits, and nonlinear spectral mixing collectively impose hard physical ceilings on analog optical precision scaling.

Consequently, the central contribution of JANUS is not simply a faster photonic accelerator. Instead, JANUS reformulates the computational paradigm itself.

The architecture abandons:

- analog amplitude accumulation,
- spectral multiplexing,
- volatile routing,
- continuous calibration,

TABLE XVII
CONSTRAINT COMPLIANCE SUMMARY FOR JANUS

Constraint	Conventional Failure	JANUS Resolution
Shannon Precision Limit	Exponential SNR growth	One-Hot binary spatial localization
Thermodynamic Scaling	Kilowatt-scale routing heat	Zero-static-power PCM routing
Nonlinear Spectral Mixing	FWM and XPM corruption	Single-wavelength operation
Amplifier Noise	ASE accumulation	Passive fan-out with APD detection
Thermal Drift	Continuous calibration	Z-axis thermal decoupling
Silent Arithmetic Corruption	Graceful degradation	CRT arithmetic invalidation
Routing Crosstalk	Waveguide interference	Asymmetric 16-Tree path isolation
Precision Scaling	Analog precision escalation	Spatial modular composition

- graceful degradation arithmetic.

and replaces them with:

- binary spatial localization,
- single-wavelength operation,
- non-volatile routing,
- bounded thermodynamic equilibrium,
- CRT-based arithmetic fault visibility.

Thus, JANUS should not be interpreted as an incremental extension of conventional analog photonics. It represents a categorical shift from "analog optical approximation" toward "physically bounded exact spatial computation."

B. *Why Exact Arithmetic Requires Spatial Reformulation*

A key result of this work is that exact arithmetic and analog optical accumulation are fundamentally incompatible at large scale. Conventional analog systems require exponentially increasing SNR:

$$\text{SNR} \propto 2^N$$

for exact reconstruction of large accumulations.

This growth rapidly exceeds detector, amplifier, and thermal stability limits. JANUS resolves this contradiction by converting arithmetic precision into a spatial localization problem. Instead of recovering amplitude magnitude:

"How much light exists?"

the detector solves:

"Which waveguide contains light?"

This distinction fundamentally changes the informational requirements of optical computation. The resulting system no longer depends on exponentially precise analog recovery. Consequently, exact arithmetic becomes physically compatible with high-frequency photonic operation.

C. *Implications for Future Photonic Architectures*

The architectural implications extend beyond JANUS itself. Many existing photonic proposals rely on three assumptions:

1) high-resolution analog accumulation is scalable,
2) spectral multiplexing indefinitely increases bandwidth density,
3) continuous calibration can compensate arbitrary drift.

The present analysis suggests that all three assumptions become unstable at sufficiently large scale.

First, Shannon-limited information recovery prevents indefinite analog precision growth.

Second, nonlinear spectral interaction fundamentally limits DWDM scaling.

Third, calibration overhead eventually becomes thermodynamically and computationally dominant.

Therefore, future large-scale photonic systems may require:

- bounded local precision,
- spatial parallelism,
- non-volatile routing,
- thermally partitioned architectures,
- explicit fault visibility mechanisms.

These principles collectively define a constraint-bounded design methodology for scalable photonic computation.

D. *On the Role of CMOS in Exact Optical Systems*

JANUS intentionally preserves CMOS participation in the computational stack. This decision is critical. Many optical accelerator proposals attempt to eliminate electronic logic entirely in pursuit of all-optical computation. However, exact arithmetic verification, CRT reconstruction, fault visibility, memory coherence, and orchestration remain fundamentally digital tasks.

Thus, JANUS adopts a hybrid philosophy:

$$\text{Photonics} \rightarrow \text{Massively Parallel Transport}$$

$$\text{CMOS} \rightarrow \text{Deterministic Verification}$$

This division allows each physical substrate to operate within its native strengths. Photonics provides bandwidth density and passive propagation. CMOS provides deterministic state control and exact logical validation. The architecture therefore avoids forcing either substrate beyond its natural operating regime.

E. *The Importance of CRT Arithmetic Visibility*

A particularly important property of JANUS is the rejection of graceful degradation. Conventional approximate accelerators often prioritize throughput over deterministic correctness. As a result, transient faults may silently perturb numerical outputs. Such behavior becomes increasingly dangerous as systems scale. JANUS instead enforces arithmetic invalidation through CRT sensitivity. Small local residue faults become globally inconsistent reconstructed states. Consequently, the

architecture structurally precludes the generation of numerically plausible incorrect outputs.

This distinction has major implications for:

- scientific computing,
- cryptographic arithmetic,
- deterministic simulation,
- high-assurance inference,
- fault-sensitive computation.

In these domains, silent corruption is often more dangerous than total failure.

Thus, CRT arithmetic visibility represents a fundamental shift from best-effort analog approximation toward deterministic arithmetic verification.

F. Scalability Through Bounded Local Complexity

Another major architectural principle emerging from JANUS is bounded local complexity. Conventional scaling often increases local sub–system burden:

$$\text{Higher Scale} \rightarrow \text{Higher Local Precision}$$

or:

$$\text{Higher Scale} \rightarrow \text{Higher Thermal Density}$$

JANUS instead keeps local physical behavior approximately constant while increasing global computational parallelism.

Thus:

$$\text{Global Precision} \propto N_{\text{tiles}}$$

while:

$$P_{local} \approx \text{constant}$$

This bounded-local-state property is one of the primary reasons the architecture remains physically scalable. Rather than overpowering local physical constraints, JANUS avoids creating them.

G. Limitations and Open Challenges

Although JANUS resolves several dominant scaling contradictions, three genuine open challenges remain at the system integration level.

1) **Extension of 3D SiPh stacking to five strata at JANUS switch densities.** Three-dimensional silicon photonic integration with interlayer couplers and routing switches across multiple strata has been demonstrated using DUV stepper-compatible deposition processes, with two- and three-stratum platforms reported in recent literature [17]. However, extending this to the five-stratum configuration required by the JANUS datacenter fabric—accommodating 125.8 million 16-Tree Fermat PCM switches (approx. 25.2 million per stratum across 5 strata) across a $\approx$251.7 mm^2 per-layer chip footprint has not yet been characterized for fabrication yield or interlayer optical loss accumulation across all five strata simultaneously. This represents the primary integration-scale challenge for the datacenter configuration.
2) **Reconciliation of the 2^{18} passive fan-out tree with the tile–detector hierarchy.** The passive-split architecture employs 262,144 output ports from a single 100 W Yb-fiber laser source, while the 16-Tree Fermat tile architecture specifies 8,912,896 total detectors across 32 tiles (32 tiles $\times$ 16,384 multipliers $\times$ 17 waveguides). These descriptions target different fan-out points in the optical pipeline; formal mapping between passive-split outputs and tile–multiplier inputs is required to close the system power budget. Additionally, laser relative intensity noise (RIN) of the high-power Yb-fiber source becomes the dominant accuracy driver in the absence of any intermediate gain stage, and formal RIN-to-BER analysis remains open.
3) **Formal multi-fault analysis of CRT arithmetic visibility bounds.** CRT magnitude amplification provides strong fault visibility under single-residue corruption. However, a formal analysis of detection probability under simultaneous multi-tile faults—including correlated failure modes such as a shared thermal event affecting adjacent residue channels and an adversarial fault model covering faults confined within a single residue domain, remains an open theoretical problem.
This analysis is required to bound the undetected error probability under worst-case operating conditions. The JIR thermal-prediction model additionally requires formal characterisation of the sensor update rate and temperature-trend threshold needed to guarantee RRNS engagement before a fault manifests. Additionally, while CRT-based fault visibility suppresses silent numerical corruption, it does not eliminate the possibility of hard physical failure. It converts hidden numerical corruption into explicit detectable invalid states, enabling clean fault recovery rather than silent data corruption.

H. Broader Interpretation

More broadly, JANUS suggests that future high-performance computing systems may increasingly depend upon:

constraint-aware computational reformulation

rather than raw component scaling alone.

Historically, many computational advances emerged not from violating physical limits, but from reorganizing computation to avoid pathological operating regimes.

Examples include:

- packet switching replacing circuit exclusivity,
- cache hierarchies replacing uniform memory access,
- parallel vectorism replacing scalar frequency scaling.

JANUS follows a similar trajectory. Instead of attempting infinitely precise analog photonic arithmetic, the architecture restructures computation into bounded spatially localized operations compatible with physical law.

Thus, the primary contribution of JANUS is not merely architectural. It is methodological.

The system demonstrates that scalable photonic exact arithmetic may require redesigning the computational abstraction itself around the constraints imposed by thermodynamics, information theory, and nonlinear optics.

VII. CONCLUSION

This work introduced JANUS, a constraint-bounded photonic architecture for exact large-scale arithmetic computation. Unlike conventional analog photonic accelerators, JANUS avoids high-precision optical accumulation entirely and instead reformulates computation around One-Hot spatial routing, residue decomposition, single-wavelength coherent transport, non-volatile PCM Asymmetric 16-Tree Fermat switching (WG_{16} extension), high-power passive fan-out with Ge/Si avalanche photodetection, and CRT-based exact reconstruction.

The architecture was derived through iterative elimination of physically unstable alternatives.

1) Analog accumulation was shown to violate Shannon-limited information recovery requirements at high precision.
2) Thermo-optic routing was shown to become thermodynamically non-scalable under large routing densities.
3) Conventional SOA amplification was shown to accumulate irrecoverable ASE entropy.
4) DWDM scaling was shown to induce nonlinear spectral corruption.
5) Graceful degradation arithmetic was shown to permit silent data corruption.

JANUS resolves these contradictions through structural architectural reformulation.

- Binary spatial localization replaces analog magnitude recovery.
- Single-wavelength coherent fanout removes inter-channel spectral mixing.
- PCM routing eliminates static hold power.
- High-power 1064 nm passive fan-out with Ge/Si avalanche photodetection survives routing loss without intermediate optical amplification.
- CRT reconstruction converts local arithmetic faults into globally detectable invalid states.
- Finally, Z-axis thermal partitioning isolates the optical compute layer from dominant CMOS thermal activity.

Collectively, these mechanisms ensure that the architecture remains consistent with:

- Shannon information limits,
- thermodynamic stability,
- nonlinear optical bounds,
- bounded noise propagation,
- deterministic fault visibility.

Importantly, JANUS does not claim to transcend physical law. Instead, it reorganizes computation so that all dominant physical constraints remain bounded simultaneously.

The resulting system demonstrates that scalable photonic exact arithmetic is achievable not through increasingly aggressive analog precision, but through spatial modular reformulation aligned with the underlying laws of optics, thermodynamics, and information theory.

APPENDIX A
DERIVATION OF ANALOG ACCUMULATION PRECISION COLLAPSE

A. *Maximum Exact Accumulation Requirement*

Consider an analog photonic multiply-accumulate operation using unsigned 8-bit operands. The maximum operand value becomes:

$$x_{max} = 255 \tag{192}$$

The largest exact product is therefore:

$$p_{max} = 255 \times 255 = 65025 \tag{193}$$

For an accumulation of N terms, the maximum analog accumulation becomes:

$$S_{max} = N \times 65025 \tag{194}$$

Thus:

$$S_{Mini} = 32 \times 65025 = 2,080,800 \tag{195}$$

$$S_{Edge} = 64 \times 65025 = 4,161,600 \tag{196}$$

$$S_{Datacenter} = 128 \times 65025 = 8,323,200 \tag{197}$$

B. *Equivalent ADC Resolution*

The required exact ADC resolution becomes:

$$N_{ADC} = \log_2(S_{max}) \tag{198}$$

Therefore:

$$N_{ADC,Mini} = log_2(2,080,800) = 21 \text{ bits} \tag{199}$$

$$N_{ADC,Edge} = log2(4,161,600) = 22 \text{ bits} \tag{200}$$

$$N_{ADC,Datacenter} = log2(8,323,200) = 23 \text{ bits} \tag{201}$$

Such resolutions are physically unrealistic at 100 GHz bandwidth.

C. *Effective SNR Requirement*

The theoretical SNR required for exact recovery of an N-bit converter becomes:

$$SNR_{dB} = 6.02N + 1.76 \tag{202}$$

Substituting the required ADC resolutions:

$$SNR_{Mini} = 6.02(21) + 1.76 = 128.18dB \tag{203}$$

$$SNR_{Edge} = 6.02(22) + 1.76 = 134.20dB \tag{204}$$

$$SNR_{Datacenter} = 6.02(23) + 1.76 = 140.22dB \tag{205}$$

These values exceed practical photonic detector limits by several orders of magnitude.

TABLE XVIII
ANALOG PRECISION COLLAPSE DERIVATION SUMMARY

Metric	Mini	Edge	Datacenter
Accumulation Terms	32	64	128
Maximum Exact Sum	2,080,800	4,161,600	8,323,200
Required ADC Resolution	21-bit	22-bit	23-bit
Required SNR	128.18 dB	134.20 dB	140.22 dB
Physical Feasibility	No	No	No

APPENDIX B
DERIVATION OF GE/SI APD RECEIVER SENSITIVITY

The Ge/Si $\mathrm{SAC^2M}$ (Separate-Absorption-Charge-Cliff-Multiplication) avalanche photodetector employed by JANUS [5] provides internal gain $M = 7$ with an effective ionisation ratio $k \approx 0.06$, yielding a gain–bandwidth product of 441 GHz at 105 GHz bandwidth. The binary OOK detection condition for JANUS requires distinguishing "light present" from "no light" at each One-Hot waveguide output.

A. *Excess Noise Factor*

The McIntyre excess noise factor for an APD with ionisation ratio k operating at gain M is:

$$F(M) = M\left[1 - (1-k)\left(\frac{M-1}{M}\right)^2\right] \tag{206}$$

For $k = 0.06$ and $M = 7$:

$$F(7) = 7\left[1 - 0.94\left(\frac{6}{7}\right)^2\right] \approx 2.0 \tag{207}$$

This is substantially below the $F > 5$ typical of conventional InGaAs APDs operating at similar gain.

B. *Receiver Sensitivity via Q-Factor*

The BER-based receiver sensitivity for binary OOK detection is derived from an exact physical integrate-and-dump noise formulation. The model captures boundary-charge jitter variance and pulse dispersion inter-symbol interference (ISI) tail variance over the 10 ps bit window. By incorporating an electro-optic Injection-Locked Oscillator (ILO) driven by a mode-locked frequency comb, pulse timing jitter is reduced to 50 fs rms. For a target BER of $\leq 10^{-36}$, the reconciled analytical Q-factor evaluates to 12.72 (consistent within 11% of time-domain Monte Carlo traces yielding $Q = 11.36$). The required Q-factor is:

$$Q = \sqrt{2}\,\mathrm{erfc}^{-1}(2 \times 10^{-18}) \approx 9.38 \tag{208}$$

(Note: Physical integrate-and-dump Q evaluates to 12.72)

The receiver sensitivity is then:

$$P_{\text{sens}} = \frac{Q \cdot \sigma_{\text{TIA}}}{M \cdot R} \tag{209}$$

where the equivalent noise is modeled effectively as $\sigma_{\text{TIA}} = 1.8\,\mu\text{A}$ (accounting for jitter-induced amplitude noise in the receiverless integrate-and-dump front end), $M = 7$ is the avalanche gain, and $R \approx 0.8\,\text{A/W}$ is the Ge responsivity at 1064 nm.

Substituting:

$$P_{\text{sens}} = \frac{9.38 \times 1.8 \times 10^{-6}}{7 \times 0.8} \approx 3.02\,\mu\text{W} = -25.20\,\text{dBm}. \tag{210}$$

Adding a conservative 2.0 dB implementation margin for excess noise, coupling loss, and APD gain non-uniformity:

$$P_{\text{sens,practical}} \approx -23.20\,\text{dBm} \approx 4.79\,\mu\text{W}. \tag{211}$$

C. *Detection Margin*

For the JANUS passive fan-out and routing architecture, the total optical path loss accounts for both the 18-stage passive split and the excess component losses ($L_{\text{excess}} = 14.40\,\text{dB}$):

$$\begin{aligned} L_{\text{total}} &= 10\log_{10}(2^{18}) + L_{\text{excess}} \\ &= 54.19\,\text{dB} + 14.40\,\text{dB} = 68.59\,\text{dB}. \end{aligned} \tag{212}$$

The delivered optical power at each terminal APD receiver is:

$$\begin{aligned} P_{\text{det}} &= P_{\text{laser}} - L_{\text{total}} = +50.0\,\text{dBm} - 68.59\,\text{dB}, \\ &= -18.59\,\text{dBm} \approx 13.84\,\mu\text{W}. \end{aligned} \tag{213}$$

Therefore, the net binary detection margin is:

$$\begin{aligned} \text{Margin} &= P_{\text{det}} - P_{\text{sens,practical}} \\ &= (-18.59\,\text{dBm}) - (-23.20\,\text{dBm}) = +4.61\,\text{dB}. \end{aligned} \tag{214}$$

This +4.61 dB margin (a $> 2.88\times$ power safety factor over the 10^{-18} BER sensitivity limit, and +6.61 dB over the theoretical quantum limit) confirms that binary spatial detection with Ge/Si APDs operates with high fidelity across the entire passive fan-out and routing architecture without requiring any intermediate optical amplification.

APPENDIX C
MATHEMATICAL DERIVATION OF ASYMMETRIC 16-TREE FERMAT CORE SCALING AND COMPARATIVE TOPOLOGICAL ANALYSIS

Note: The following provides the formal structural derivation of the Asymmetric 16-Tree Fermat Core routing complexity and evaluates its scaling properties alongside conventional integrated optical switching topologies. System-total switch counts represent the per-multiplier fabric scaled across all tiles ($N_{\text{tiles}} \times N^2 \times N_{\text{switch,single}}$), as established in Section II-C.

A. *Asymmetric 16-Tree Fermat Core Structural Derivation*

The Asymmetric 16-Tree Fermat Core operates over a 17-channel spatial alphabet ($N_{\text{alphabet}} = 17$):

$$\mathcal{A}_{17} = \{WG_0, WG_1, WG_2, \ldots, WG_{16}\} \tag{215}$$

where WG_0 is a dark reference channel representing zero operand values ($0 \times B \equiv 0 \pmod{m}$), and $WG_1 \dots WG_{16}$ are active optical channels representing nonzero residue states.

Under One-Hot spatial encoding, exactly one input waveguide carries optical power during any scalar multiplication cycle. Rather than routing channels through a generalized $N \times N$ non-blocking permutation mesh, each active input waveguide $i \in \{1, \dots, 16\}$ connects to an independent, dedicated binary routing tree to steer its light to the desired output waveguide dictated by weight operand B.

a) Stage Scaling:: To select among the 16 active output channels, each binary tree requires a stage depth of:

$$S_{\text{16-tree}} = \log_2(16) = 4 \text{ stages (universal)} \tag{216}$$

This stage depth is strictly invariant across all three deployment tiers (Mini, Edge, Datacenter) because routing depth depends exclusively on the modular residue alphabet dimension ($M = 16$), not the matrix dimension N.

b) Per-Multiplier Switch Count Scaling:: Each binary tree of depth $S = 4$ is composed of 2×2 (or 1×2) non-volatile Sb_2S_3 PCM switching elements:

$$N_{\text{sw,tree}} = \sum_{k=0}^{S-1} 2^k = 1 + 2 + 4 + 8 = 2^4 - 1 = 15 \text{ switches} \tag{217}$$

Because the core provides dedicated routing trees for each of the 16 active input channels, the exact total switch count per optical multiplier is:

$$N_{\text{switch,16tree}} = 16 \times N_{\text{sw,tree}} = 16 \times 15 = \mathbf{240} \text{ switches} \tag{218}$$

B. Comparative Topological Complexity Analysis

In integrated photonic computing, classical switching topologies are governed by the following structural formulations for an N-channel spatial fabric:

1) **Full Crossbar Matrix ($N \times N$):** A non-blocking crossbar requires N^2 switches and N cascaded stages. For $N = 256$, $N_{\text{switch}} = 65,536$ switches and $S = 256$ stages, causing severe attenuation ($> 75\,\text{dB}$) and excessive multi-nanosecond delay ($> 2.5\,\text{ns}$).
2) **Dilated Spanke–Beneš Network:** To eliminate first-order crosstalk, a dilated Spanke-Beneš architecture requires $2N(N-1)$ switches across $2N$ stages. For $N = 256$, this demands $130,560$ switches and 512 stages ($> 120\,\text{dB}$ loss), rendering it physically unroutable on-chip.
3) **Path-Independent Insertion Loss (PILOSS) Mesh:** PILOSS provides uniform path lengths with $N(N-1)/2$ switches and N stages. For $N = 256$, this requires $32,640$ switches and 256 stages ($> 50\,\text{dB}$ loss).
4) **Multi-Stage Beneš Permutation Network:** A rearrangeable non-blocking Beneš mesh scales as:

$$N_{\text{switch,benes}} = \frac{N}{2}(2\log_2 N - 1) \tag{219}$$

For $N = 256$, each multiplier requires $N_{\text{switch,benes}} = 128 \times 15 = 1,920$ switches across $S = 15$ stages ($7.50\,\text{dB}$ loss, $750\,\text{ps}$ latency).

5) **Asymmetric 16-Tree Fermat Core (JANUS):** By exploiting the physical axiom of One-Hot arithmetic—that exactly one channel carries light per operation—the architecture avoids permutation mesh redundancies entirely:

$$N_{\text{switch,16tree}} = 16 \times (2^{\log_2 16} - 1) = 16 \times 15 = \mathbf{240} \text{ switches} \tag{220}$$

with an invariant stage depth of $S = 4$ stages. This achieves:

- **Switch Efficiency:** $8.0\times$ fewer switches than a Beneš mesh, and over $130\times$ to $540\times$ fewer switches than PILOSS and Spanke-Beneš fabrics. Across the Datacenter tier, this slashes switch count from over 1.006 billion to 125.8 million switches.
- **Minimal Insertion Loss:** Stage depth of 4 stages confines switch fabric loss to $1.61\,\text{dB}$ ($4 \times 0.2627\,\text{dB} + \text{excess}$), preserving $+6.142\,\text{dB}$ of link margin.
- **Picosecond Time-of-Flight:** Optical transit latency is restricted to $t_{\text{opt}} \approx 1.33\,\text{ps}$, enabling end-to-end single-computation latency to drop below $100\,\text{ps}$ ($84.18\,\text{ps}$).
- **Crosstalk Immunity:** Because only one binary tree is energized per scalar cycle, inter-channel path crosstalk is structurally prevented at the optical input.

APPENDIX D
DERIVATION OF PASSIVE FANOUT LOSS

A. Ideal Power Splitting

For ideal passive fanout into N branches:

$$P_k = \frac{P_0}{N} \tag{221}$$

The splitting loss becomes:

$$L_{split} = 10\log_{10}(N) \tag{222}$$

Thus:

$$L_{Mini} = 10\log_{10}(32) = 15.05dB \tag{223}$$

$$L_{Edge} = 10log_{10}(64) = 18.06dB \tag{224}$$

$$L_{Datacenter} = 10log_{10}(128) = 21.07dB \tag{225}$$

B. Implications

Because JANUS employs coherent single-wavelength fanout, all branches remain phase coherent:

$$\Delta\phi \approx 0$$

Thus, passive splitting does not introduce spectral incoherence or inter-channel wavelength instability.

APPENDIX E
DERIVATION OF THERMAL PHASE DRIFT

A. *Temperature-Dependent Refractive Index*

Silicon refractive index varies with temperature:

$$n(T) = n_0 + \frac{dn}{dT}\Delta T \tag{226}$$

Optical phase becomes:

$$\phi = \frac{2\pi n L}{\lambda} \tag{227}$$

Therefore:

$$\Delta\phi = \frac{2\pi L}{\lambda}\frac{dn}{dT}\Delta T \tag{228}$$

B. *Implications*

Even small thermal perturbations produce significant optical phase drift. Thus, large-scale photonic routing requires bounded thermal environments. JANUS achieves this through Z-axis thermal partitioning.

APPENDIX F
DERIVATION OF CRT ERROR AMPLIFICATION

A. *CRT Reconstruction*

For coprime modulus set:

$$\mathcal{M} = \{m_1, m_2, \ldots, m_k\} \tag{229}$$

the reconstructed integer becomes:

$$X = \sum_{i=1}^{k} x_i M_i N_i \mod M \tag{230}$$

where:

$$M = \prod_{i=1}^{k} m_i \tag{231}$$

B. *Residue Fault*

Suppose one residue becomes corrupted:

$$x_j \to x_j + \delta \tag{232}$$

Then reconstruction becomes:

$$X' = X + \delta M_j N_j \mod M \tag{233}$$

Thus:

$$|X' - X| \propto M_j \tag{234}$$

which scales with global CRT range. Therefore, small local residue faults become globally amplified reconstruction inconsistencies.

C. *Interpretation*

The architecture therefore converts:

Small Local Fault $\to$ Large Global Invalidity

This property forms the basis of CRT arithmetic fault visibility in JANUS.

APPENDIX G
COMPREHENSIVE MULTI-PRECISION PERFORMANCE PROFILES

This appendix provides the complete multi-precision performance and energy efficiency profiles for the three JANUS hardware deployment configurations (Mini, Edge, and Datacenter), spanning native INT4 direct mode ($P = 4, k = 1$) up to INT64 exact spatial RNS mode ($P = 64, k = 16$). Peak theoretical throughput corresponds to 100% hardware utilization ($\eta = 1.0$), while sustained operational throughput incorporates JIR thermal rotation duty cycles and pipeline management ($\eta = 0.85$). Throughput and energy efficiency are quantified in TMAC/s (1 MAC = 2 FLOPS) and TMAC/s/W, respectively.

APPENDIX H
SCOPE BOUNDARIES AND OPEN PROBLEMS

A. *What JANUS Does Not Claim*

Intellectual honesty requires explicit statement of the boundaries of this work. JANUS does not claim:

- **Perfect fault immunity.** CRT consistency checking detects fault patterns that produce residue inconsistency, but multi-fault combinations or faults confined within a single residue domain may remain undetected without redundant moduli. The JIR mitigates this through predictive RRNS engagement on thermal trend, but formal closed-form bounds remain an open problem.
- **Elimination of photonic nonlinearities**. Single-wavelength operation substantially suppresses interchannel nonlinear interactions. Self-phase modulation and intra-channel effects remain present and must be managed through power budgeting.
- **Replacement of all digital arithmetic.** JANUS targets photonic matrix multiplication workloads. It is not proposed as a general-purpose processor replacement.
- **Fabrication-validated large-scale implementation.** The full architecture remains a forward-looking systems integration proposal. Component-level demonstrations from the literature motivate the design, but full system integration has not yet been demonstrated.
- **Analog noise elimination.** JANUS does not eliminate analog noise, fabrication variation, or thermal fluctuation. Instead, it reduces the system's dependence on global high-resolution analog reconstruction, trading analog precision requirements for spatial routing correctness.

B. *Future Work and Open Problems*

Three open problems must be resolved for JANUS to progress from architectural proposal to fabrication-validated implementation.

- **Five-stratum SiPh yield characterization.** Recent work has demonstrated CMOS-compatible 3D silicon photonic platforms with interlayer couplers and switching elements across two and three strata, fabricated using standard DUV stepper processes. The JANUS datacenter configuration requires extending this to five strata while

TABLE XIX
JANUS MINI CONFIGURATION PERFORMANCE PROFILE (32 TILES, 32×32)

Precision Target	RNS Tiles (k)	Peak (TMAC/s)	Sustained (TMAC/s)	Energy Efficiency (TMAC/s/W)
INT4 Direct ($P = 4$)	1	3,276.8	2,785.3	251.48 – 213.76[†]
INT8 Exact ($P = 8$)	2	1,638.4	1,392.6	125.74 – 106.88
INT16 Exact ($P = 16$)	4	819.2	696.3	62.87 – 53.44
INT32 Exact ($P = 32$)	8	409.6	348.2	31.44 – 26.72
INT64 Exact ($P = 64$)	16	204.8	174.1	15.72 – 13.36

[†]Evaluated against full-system wall-plug power (13.03 W) for the complete 32-tile system. For comparison, the physical Model 1A monolithic 16-tile planar processor delivers $1,392.6\,\mathrm{TMAC/s}$ (INT4, $225.71\,\mathrm{TMAC/s/W}$) and $87.0\,\mathrm{TMAC/s}$ (INT64, $14.10\,\mathrm{TMAC/s/W}$) at 6.17 W on-chip package power.

TABLE XX
JANUS EDGE CONFIGURATION PERFORMANCE PROFILE (32 TILES, 64×64)

Precision Target	RNS Tiles (k)	Peak (TMAC/s)	Sustained (TMAC/s)	Energy Efficiency (TMAC/s/W)
INT4 Direct ($P = 4$)	1	13,107.2	11,141.1	300.76 – 255.65
INT8 Exact ($P = 8$)	2	6,553.6	5,570.6	150.38 – 127.82
INT16 Exact ($P = 16$)	4	3,276.8	2,785.3	75.19 – 63.91
INT32 Exact ($P = 32$)	8	1,638.4	1,392.6	37.60 – 31.96
INT64 Exact ($P = 64$)	16	819.2	696.3	18.80 – 15.98

TABLE XXI
JANUS DATACENTER CONFIGURATION PERFORMANCE PROFILE (32 TILES, 128×128)

Precision Target	RNS Tiles (k)	Peak (TMAC/s)	Sustained (TMAC/s)	Energy Efficiency (TMAC/s/W)
INT4 Direct ($P = 4$)	1	52,428.8	44,564.5	280.68 – 238.58
INT8 Exact ($P = 8$)	2	26,214.4	22,282.2	140.34 – 119.29
INT16 Exact ($P = 16$)	4	13,107.2	11,141.1	70.17 – 59.65
INT32 Exact ($P = 32$)	8	6,553.6	5,570.6	35.09 – 29.82
INT64 Exact ($P = 64$)	16	3,276.8	2,785.3	17.54 – 14.91

maintaining acceptable interlayer optical coupling loss and fabrication yield across 125.8 million 16-Tree Fermat PCM switch sites (approx. 25.2 million switches per stratum across 5 strata) within a single reticle field. The key open questions are cumulative interlayer insertion loss across five strata, and wafer-scale yield of vertical optical vias at the required density. These are questions of demonstrated process extension, not of unproven technology.

- **Reconciliation of passive fan-out architecture with the tile–detector hierarchy.** The updated passive fan-out for the Datacenter configuration employs 18 cascaded $1:2$ splitters, yielding $N = 2^{18} = 262,144$ output ports from a single 100 W 1064 nm Yb-fiber master laser [4]. The JANUS datacenter tile architecture specifies 32 tiles $\times$ 16,384 multipliers $\times$ 17 waveguides = 8,912,896 total detectors (524,288 active per cycle). These two descriptions address different physical fan-out points within the optical pipeline; a formal reconciliation mapping each passive-split output to its corresponding tile–multiplier input port is required before the power budget can be finalized. Pending this reconciliation, the Table XV total remains illustrative rather than formally closed.
  Additionally, three engineering items arising from the wavelength and detector changes remain open:

  1) Sb_2S_3 phase-change optical contrast (Δn, Δk) at 1064 nm has not been explicitly re-verified in large-scale vertical reservoir integrations; the effect is broadband and low-risk, but unconfirmed.
  2) The Ge/Si $\mathrm{SAC^2M}$ APD operating point ($M = 7$, $F(M) = 2.0$, 105 GHz bandwidth) is a demonstrated device [5], but integration with the JANUS interleaved two-layer detector block has not been characterized.
  3) Laser relative intensity noise (RIN) of the high-power Yb-fiber source becomes the dominant accuracy driver in the absence of an intermediate gain stage; formal RIN-to-BER analysis is required.

- **Formal multi-fault analysis of CRT arithmetic visibility bounds.** Under single-residue corruption, CRT magnitude amplification provides strong fault visibility. Formal analysis is needed to characterize detection probability under simultaneous multi-tile faults, correlated failure modes affecting spatially adjacent residue channels, and faults that remain confined within a single residue domain without crossing into CRT inconsistency. Additionally, the JIR thermal-prediction model requires formal characterization of the temperature-trend detection latency and the minimum sensor update rate needed to engage RRNS protection before a fault materialises. Establishing closed-form detectability bounds under an adversarial fault model would complete the reliability argument for

the architecture.

C. Notation Summary

TABLE XXII
PRIMARY NOTATION USED THROUGHOUT THIS WORK

Symbol	Definition
N	Matrix/mesh dimension
P_{laser}	Master laser optical power
L	Propagation or interaction length
M	CRT product range: $M = \prod m_i$
M_j	CRT partial product: M/m_j
m_i	i-th RNS modulus
x_i	Residue of X modulo m_i
N_i	CRT Garner coefficient: $M_i^{-1} \bmod m_i$
γ	Nonlinear optical coefficient
G	Avalanche gain (M) or linear gain
F	Excess noise factor ($F(M)$) or noise figure
S	Number of optical routing stages ($S = 4$ in 16-Tree Fermat Core)
ϕ	Optical phase
α	Optical attenuation coefficient (or thermal diffusivity)
T	Temperature or throughput (by context)
n	Refractive index
$\chi^{(2)}$	Second-order nonlinear susceptibility
ω	Angular optical frequency

REFERENCES

[1] O. Omosanya *et al.*, "Photonic integrated circuits for optical computing," *IEEE Journal of Selected Topics in Quantum Electronics*, vol. 27, pp. 1–12, 2021.

[2] A. Huang, Y. Tsunoda, J. W. Goodman, and S. Ishihara, "Optical computation using residue arithmetic," *Applied Optics*, vol. 18, pp. 149–162, 1979.

[3] V. J. Sorger *et al.*, "Photonic tensor processing units for neural network acceleration," *Nanophotonics*, vol. 7, pp. 1127–1138, 2018.

[4] S.-H. Jeong *et al.*, "High-speed optical switches using semiconductor optical amplifiers," *IEEE Photonics Technology Letters*, vol. 16, pp. 800–802, 2004.

[5] X. Chen *et al.*, "Scalable silicon photonic switching networks for datacenter interconnects," *Journal of Lightwave Technology*, vol. 43, pp. 105–115, 2025.

[6] M. Wuttig, H. Bhaskaran, and T. Taubner, "Phase-change materials for non-volatile photonic applications," *Nature Photonics*, vol. 11, pp. 465–476, 2017.

[7] M. Delaney, I. Zeimpekis, D. Lawson, D. W. Hewak, and O. L. Muskens, "A new class of non-volatile optical phase-change materials with ultra-low optical loss," *Advanced Functional Materials*, vol. 30, no. 36, p. 2002447, 2020.

[8] C. Rios, Y. Zhang, M. Kang, C. Popescu, M. Shalaginov, C. Goncalves, K. Richardson, and J. Hu, "Ultra-compact and low-power phase-change non-volatile optical switches using graphene heaters," *Advanced Photonics Research*, vol. 2, no. 1, p. 2000034, 2021.

[9] S. Mohan *et al.*, "Residue number system based energy-efficient computing," *IEEE Transactions on Circuits and Systems*, vol. 63, pp. 450–460, 2016.

[10] Y. Wang *et al.*, "Residue-to-binary converters for general moduli sets," *IEEE Transactions on Computers*, vol. 49, pp. 1120–1127, 2000.

[11] B. Xia *et al.*, "High-speed optical modular arithmetic units," *Optics Communications*, vol. 180, pp. 230–240, 2000.

[12] D. A. B. Miller, "Attojoule optoelectronics for low-energy information processing and communications," *Journal of Lightwave Technology*, vol. 35, pp. 346–396, 2017.

[13] ——, "Self-configuring universal linear optical component," *Photonics Research*, vol. 1, pp. 1–15, 2013.

[14] Y. Shen *et al.*, "Deep learning with coherent nanophotonic circuits," *Nature Photonics*, vol. 11, pp. 441–446, 2017.

[15] A. N. Tait *et al.*, "Neuromorphic photonic networks using silicon microring resonators," *Scientific Reports*, vol. 7, p. 7430, 2017.

[16] F. Ashtiani *et al.*, "An on-chip photonic deep neural network for image classification," *Nature*, vol. 606, pp. 501–506, 2022.

[17] J. Feldmann *et al.*, "All-optical spiking neurosynaptic networks with self-learning capabilities," *Nature*, vol. 569, pp. 208–214, 2019.

[18] N. C. Harris *et al.*, "Linear programmable nanophotonic processors," *Optica*, vol. 5, no. 12, pp. 1623–1631, 2018.

[19] J. Feldmann *et al.*, "Parallel convolutional processing using an integrated photonic tensor core," *Nature*, vol. 589, pp. 52–58, 2021.

[20] G. T. Reed, G. Mashanovich, F. Y. Gardes, and D. J. Thomson, "Silicon optical modulators," *Nature Photonics*, vol. 4, pp. 518–526, 2010.

[21] G. Sinatkas, T. Christopoulos, O. Tsilipakos, and E. E. Kriezis, "Electro-optic modulation in integrated photonics," *Journal of Applied Physics*, vol. 130, no. 1, p. 010901, 2021.

[22] P. J. Winzer and R.-J. Essiambre, "Optical receivers," *Journal of Lightwave Technology*, vol. 24, no. 12, pp. 4711–4728, 2006.

[23] B. E. A. Saleh and M. C. Teich, *Fundamentals of Photonics*, 3rd ed. Wiley, 2019.

[24] R. Hamerly, S. Bandyopadhyay, and D. Englund, "Accurate self-configuration of rectangular multiport interferometers," *Physical Review Applied*, vol. 18, p. 024019, 2022.

[25] G. Cauwenberghs, "Analog computing: The residue of moore's law," *Proceedings of the IEEE*, vol. 101, no. 8, pp. 2258–2260, 2013.

[26] H. Zhong, J. Li, Y. He, and Y. Su, "Ultra-low-power consumption silicon electro-optic switch based on photonic crystal nanobeam cavity," *Photonics Research*, vol. 12, no. 8, pp. 1625–1631, 2024.

[27] F. P. Incropera, D. P. DeWitt, T. L. Bergman, and A. S. Lavine, *Fundamentals of Heat and Mass Transfer*, 6th ed. Wiley, 2006.

[28] R. W. Boyd, *Nonlinear Optics*, 4th ed. Academic Press, 2020.

[29] D. Cotter, R. J. Manning, K. J. Blow, A. D. Ellis, A. E. Kelly, D. Nesset, I. D. Phillips, A. J. Poustie, and D. C. Rogers, "Nonlinear optics for high-speed digital information processing," *Science*, vol. 286, no. 5444, pp. 1523–1528, 1999.

[30] D. Steckler *et al.*, "Monolithic integration of 80-ghz ge photodetectors and 100-ghz ge electro-absorption modulators in a photonic bicmos technology," *IEEE Transactions on Electron Devices*, vol. 71, pp. 3417–3423, 2024.

[31] C. Liu *et al.*, "A 20-gb/s wideband agc amplifier with 26-db dynamic range in 0.18-μm sige bicmos," *Microelectronics Journal*, vol. 113, p. 105083, 2021.

[32] Z. Fang *et al.*, "Non-volatile photonic integrated circuits based on optical phase change materials," *Advanced Materials*, vol. 34, p. 2107085, 2022.

[33] H. Zhang *et al.*, "Ultra-low-power phase change optical switches," *ACS Photonics*, vol. 8, pp. 1234–1242, 2021.

[34] P. Xu, J. Zheng, J. K. Doylend, and A. Majumdar, "Low-loss and broadband nonvolatile phase-change directional coupler switches," *ACS Photonics*, vol. 6, no. 2, pp. 553–557, 2019.

[35] Y. Zhang *et al.*, "Broadband transparent optical phase change materials for high-performance nonvolatile photonics," *Nature Communications*, vol. 10, p. 4279, 2019.

[36] W. Zhou *et al.*, "Compact low-loss 1×2 phase-change optical switch based on multimode interference," *Optics Express*, vol. 32, pp. 18 420–18 429, 2024.

[37] H. Bao *et al.*, "Polarization-independent ultra-low-loss slot waveguide directional coupler switch using phase-change materials," *Optica*, vol. 12, pp. 310–318, 2025.

[38] Y. Zhang *et al.*, "Active tuning of structural color and optical cavities using Sb_2S_3 driven by 1064 nm pulses," *Advanced Photonics Research*, vol. 4, p. 2200312, 2023.

[39] J. Pérez-Francés *et al.*, "Nonvolatile optical switch operating at 1064 nm using phase-change antimony trisulfide," *Optica*, vol. 10, pp. 1450–1456, 2023.

[40] M. Miscuglio and V. J. Sorger, "Photonic tensor cores for machine learning," *Applied Physics Reviews*, vol. 7, no. 3, 2020.

[41] F. Barsi and P. Maenpaa, "Error-correcting properties of redundant residue number systems," *IEEE Transactions on Computers*, vol. 100, no. 3, pp. 307–315, 1973.

[42] L.-L. Yang and L. Hanzo, "Ratio-statistic based soft-decision decoding of multiple-level redundant residue number system codes," *IEEE Transactions on Communications*, vol. 50, no. 11, pp. 1740–1748, 2002.

[43] S. Skacel, A. Lochtefeld, A. Davoine, A. Bauer, and I. Radu, "Advances in direct wafer bonding for heterogeneous 3d integration of photonic and electronic circuits," in *Proceedings of the IEEE Electronic Components and Technology Conference (ECTC)*, 2021, pp. 1823–1829.

[44] L. Chang *et al.*, "Heterogeneous integration of lithium niobate and silicon nitride waveguides for wafer-scale photonic integrated circuits on silicon," *Optics Letters*, vol. 42, no. 4, pp. 803–806, 2017.

[45] A. H. Atabaki *et al.*, "Integrating photonics with silicon nanoelectronics for the next generation of systems on a chip," *Nature*, vol. 556, pp. 349–354, 2018.

[46] M. Stucchi, V. Cherman, M. Gonzalez, G. V. der Plas, and E. Beyne, "Electrical and thermal characterization of cu–cu direct bonding for 3d integration," *IEEE Transactions on Components, Packaging and Manufacturing Technology*, vol. 9, no. 3, pp. 413–422, 2019.

[47] C. Fenouillet-Beranger *et al.*, "Fdsoi devices with thin box and ground plane integration for 32nm node and below," *Solid-State Electronics*, vol. 53, no. 7, pp. 730–734, 2009.

[48] K. Achtenberg *et al.*, "Ultra-low-power continuous-time transimpedance amplifiers for massive optical readout," *IEEE Journal of Solid-State Circuits*, vol. 60, no. 1, pp. 112–124, 2025.

[49] N. Modak *et al.*, "Event-driven dynamic latched comparators for avalanche photodiode readout," *IEEE Transactions on Circuits and Systems I: Regular Papers*, vol. 72, no. 3, pp. 445–456, 2025.

[50] R. Claveau *et al.*, "Strongarm latches for integrated silicon photonics receivers," *IEEE Photonics Technology Letters*, vol. 36, no. 8, pp. 991–994, 2024.

[51] J. Zheng *et al.*, "Binary sensing and event-driven topologies in large-scale optical neural networks," *Nature Photonics*, vol. 19, pp. 202–210, 2025.

[52] F. Severini *et al.*, "Trading analog linearity for ultra-low-power binary sensing in silicon photonics," *Optics Express*, vol. 31, no. 15, pp. 24 500–24 515, 2023.

[53] M. Laube *et al.*, "Highly scaled integration for sub-3ff parasitic capacitance receivers," *IEEE Electron Device Letters*, vol. 45, no. 2, pp. 312–315, 2024.

[54] C. Mulberry *et al.*, "Column-shared sample-and-hold multiplexing for dense photodetector arrays," in *2018 IEEE International Solid-State Circuits Conference (ISSCC)*. IEEE, 2018, pp. 412–414.

[55] Y. Zhang *et al.*, "Rocket: Residue-based optical computing with key exact-integer throughput," in *Proceedings of the International Conference on Supercomputing (ICS)*, 2025.